



# ORIGIN AND CHARACTERIZATION OF THE LITHOFACIES AND DUAL MICROPORE/MACROPORE NETWORK IN PENNSYLVANIAN (EARLY DESMOINESIAN) CADDO SHELF-BUILDUP COMPLEXES, STEPHENS COUNTY, NORTH-CENTRAL TEXAS

Robert G. Loucks and Qilong Fu

*Bureau of Economic Geology, Jackson School of Geosciences, University of Texas at Austin,  
University Station, Box X, Austin, Texas 78713–8924, U.S.A.*

## ABSTRACT

The Pennsylvanian (early Desmoinesian) Caddo Formation in north-central Texas contains shelf carbonate buildups composed of phylloid algal and *Komia* allochems with early cementation and microbial binding. Cores from the Caddo reservoirs have a dual pore network composed of macro- and micropores. The macropores are original interparticle and intraparticle pores, as well as moldic and vuggy pores associated with the dissolution of aragonite allochems. The micropores are produced by the transformation of Mg–calcite allochems, micrite rims, and peloidal muds to calcite. Porosity ranges between 0.8% and 25.1%, and permeability ranges between 0.01 md and 370.5 md. The phylloid algal facies and *Komia* facies have the best reservoir quality. The presence of micropores must be considered when analyzing porosity-permeability transforms, hydrocarbon saturation, and reservoir reserves.

## INTRODUCTION

Micropores appear to be a very common component of pore networks in Paleozoic limestones, and the early Desmoinesian Caddo Formation in north-central Texas (Figs. 1 and 2) is an excellent example of where a dual pore network composed of macropores and micropores forms economic reservoirs. The Caddo reservoirs are associated with shelf-buildup complexes composed predominantly of phylloid algae and *Komia*, which has been defined as a calcareous red algae (Johnson, 1961). The macropores are original interparticle and intraparticle pores, as well as moldic and vuggy pores associated with the dissolution of aragonite allochems. Micropores are a transformation product of former Mg–calcite allochems, micrite envelopes, and lime peloidal mud (peloids may be associated with cyanobacteria microbialites). Micropores in the Paleozoic have not been well documented except by a few authors (e.g., Kopaska-Merkel, 1988; Kaldi et al., 1990; Wahlman, 2009; Wood, 2013; Loucks and Ulrich, 2015), and the micropores in the Caddo Limestone have been overlooked by several authors (e.g., Forehand, 1991; Weber, 1995; Miller, 2001) who have described the Caddo reservoirs.

Specific research objectives include: (1) defining the lithofacies and associated allochems in the Caddo Limestone; (2) interpreting the depositional setting and providing a depositional model of the phylloid algal and *Komia* shelf-buildup complexes and deposits in Stephens County, Texas; (3) outlining the general diagenesis of the Caddo Limestone; (4) delineating the origin of the micropores; and (5) providing a characterization of the macropore/micropore network.

## DATA AND METHODS

The rock and wireline-log data for this study come from the Texas Pacific Newell-Dell No. WI-2 and Sun Veale Parks Caddo Unit No. 36 cores in Stephens County, Texas (Figs. 1, 3, and 4). The cores were slabbed and etched with dilute HCl acid to clean the face of the carbonate core to better view rock texture and fabric. The cores were described using a binocular microscope. To highlight macropores (>10  $\mu\text{m}$ ) and to delineate micropores (<10  $\mu\text{m}$ ) under fluorescent-light microscopy, 69 thin sections impregnated with blue fluorescent-dyed epoxy were analyzed.

The cores were examined to define mineralogy, allochems, major diagenetic features, and pore types. The Dunham (1962) classification for carbonate textures was used to help describe lithofacies. Several samples were viewed using an FEI Nova NanoSEM 430 at the University of Texas at Austin. Use of this field-emission scanning electron microscope (FESEM) equipped with in-lens secondary electron detectors provided greatly enhanced detail of nanometer-scale features. Lower

Figure 1. Location of study area and cores used in this investigation.

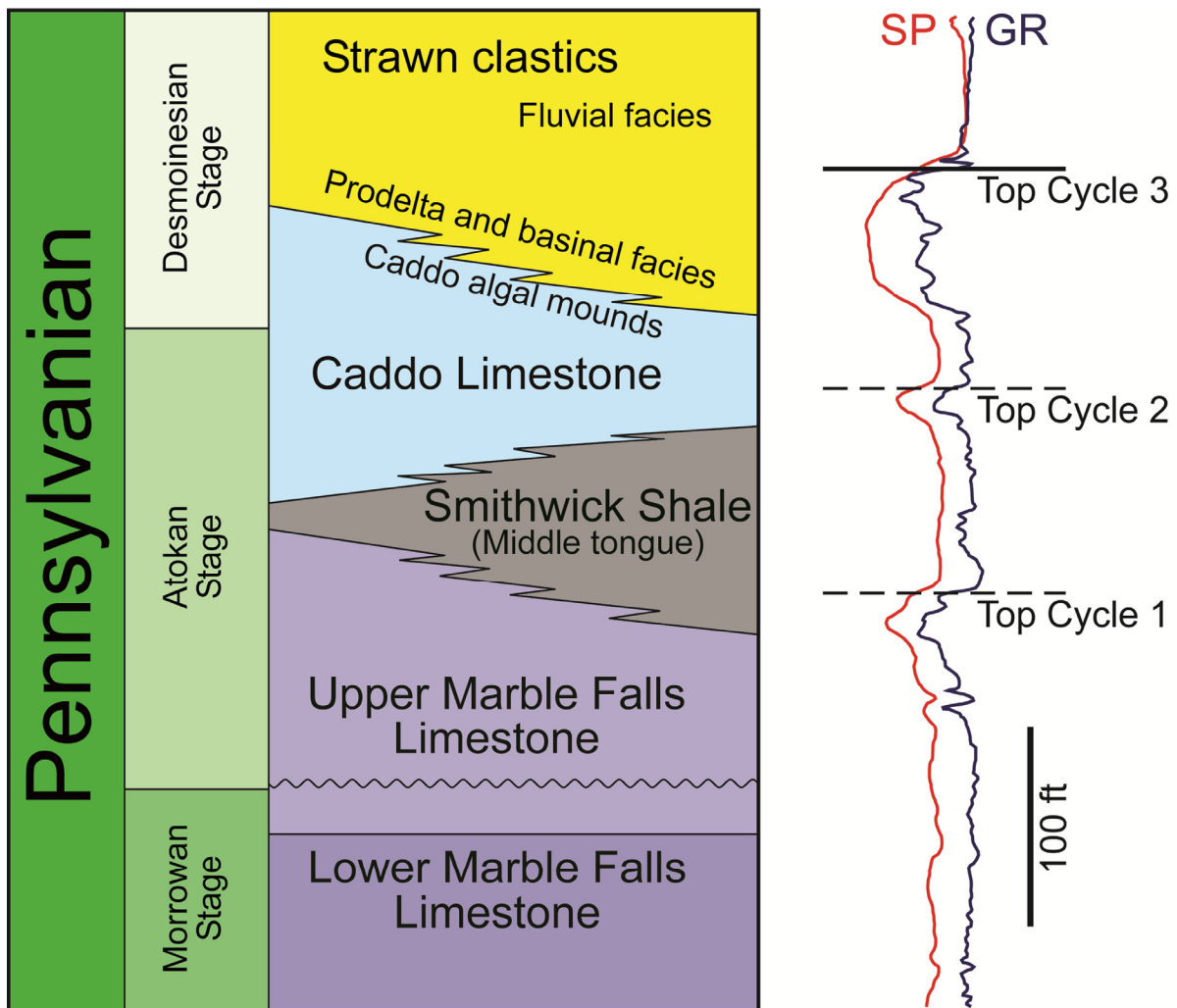
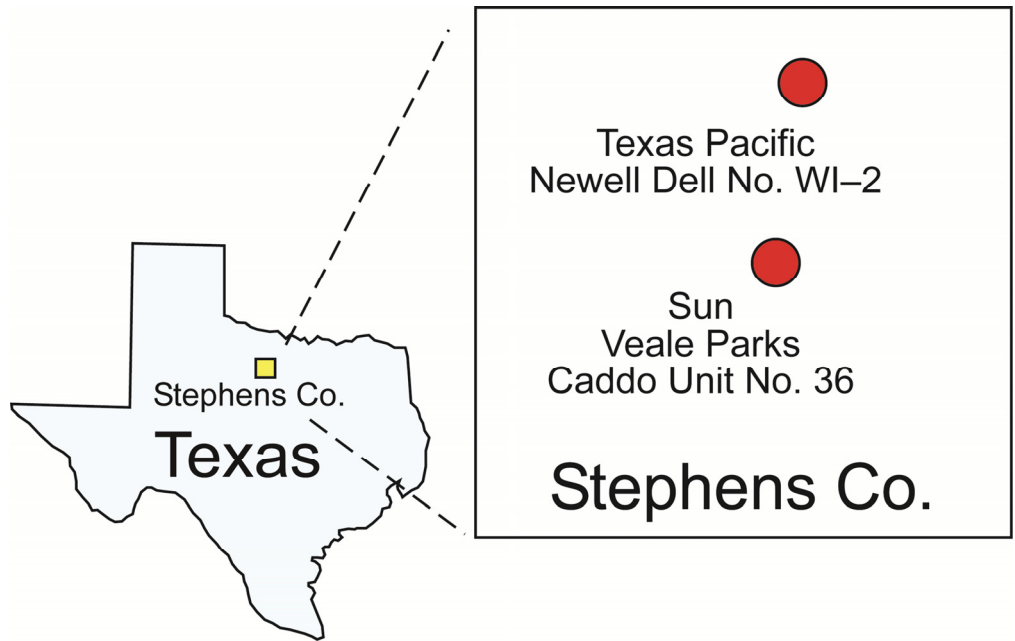


Figure 2. Pennsylvanian stratigraphic section in Stephens County, Texas. Caddo mound complexes are early Desmoinesian in age (modified after Miller, 2001). Spontaneous potential (SP) and gamma ray (GR) log curves from Newell Dell No. WI-2 well. Wireline log shows top Caddo Limestone and cycle tops.

Measured Section / Well: Texas Pacific Newell Dell No. WI-2

Location: Stephens County, Texas

Stratigraphic Interval: Upper section of Caddo Limestone

Logged By: Bob Loucks and Qilong Fu

Date: Sept. 2014

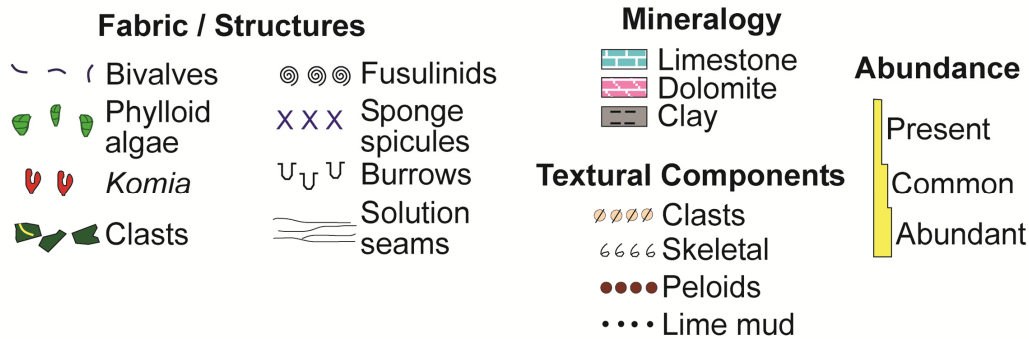
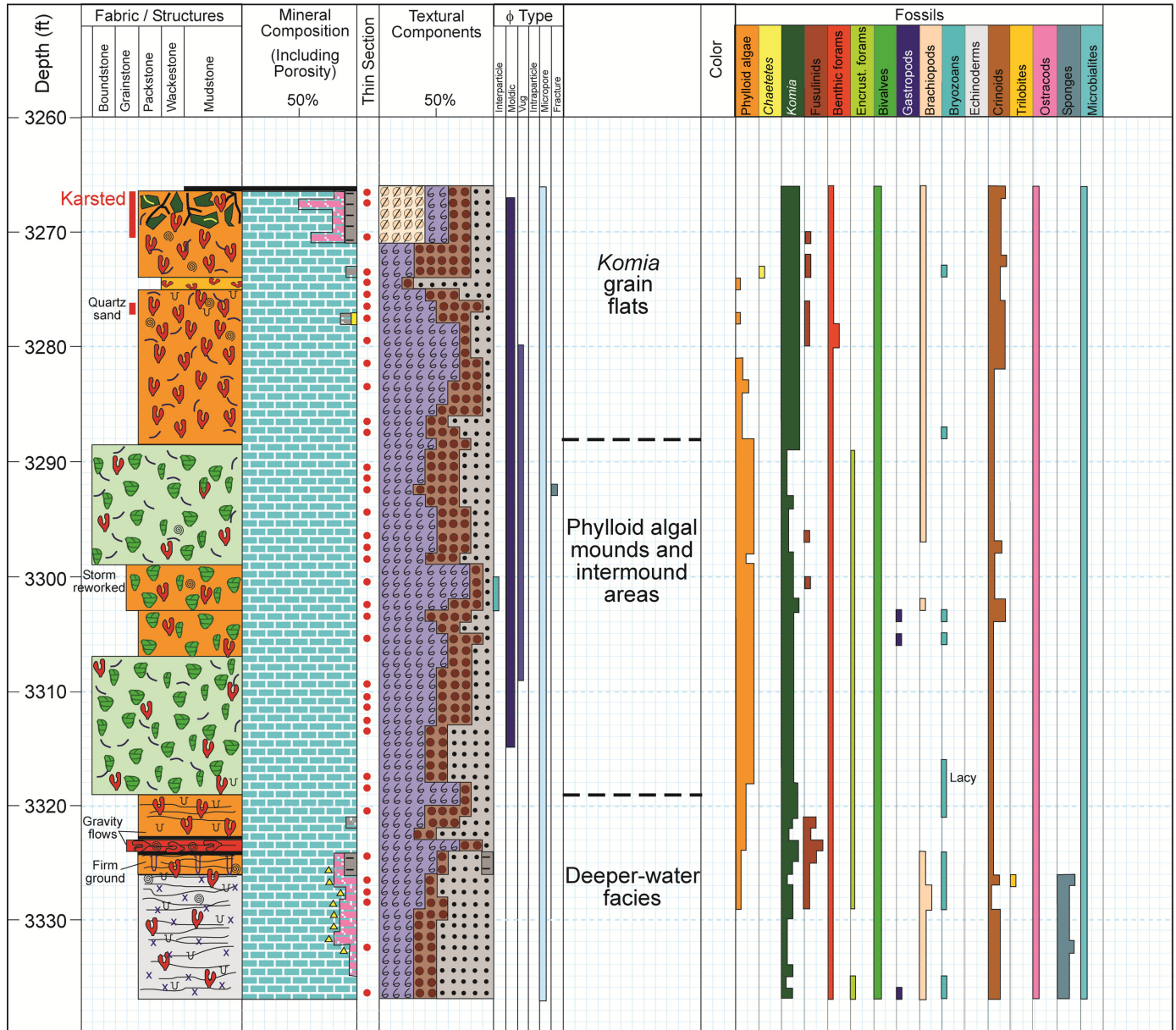


Figure 3. Core description of Texas Pacific Newell Dell No. WI-2 core.

Measured Section / Well: Sun Oil Caddo Unit Veale Parks No. 36

Location: Stephens County, Texas

Stratigraphic Interval: Upper section of Caddo Limestone

Logged By: Bob Loucks and Qilong Fu

Date: Sept. 2014

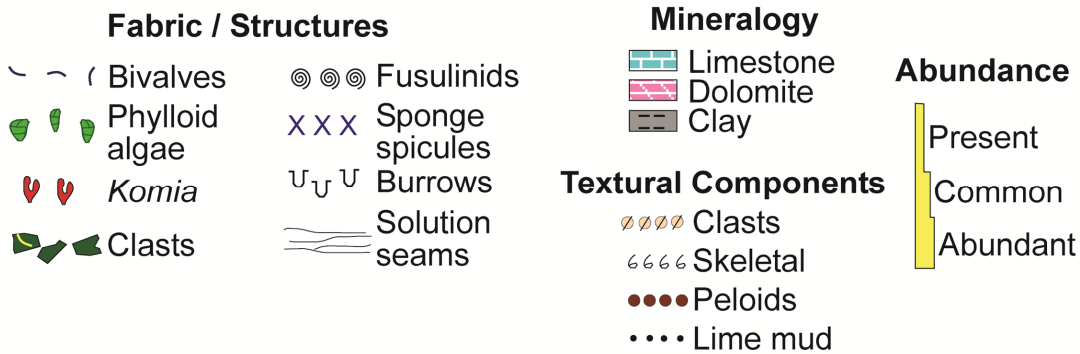
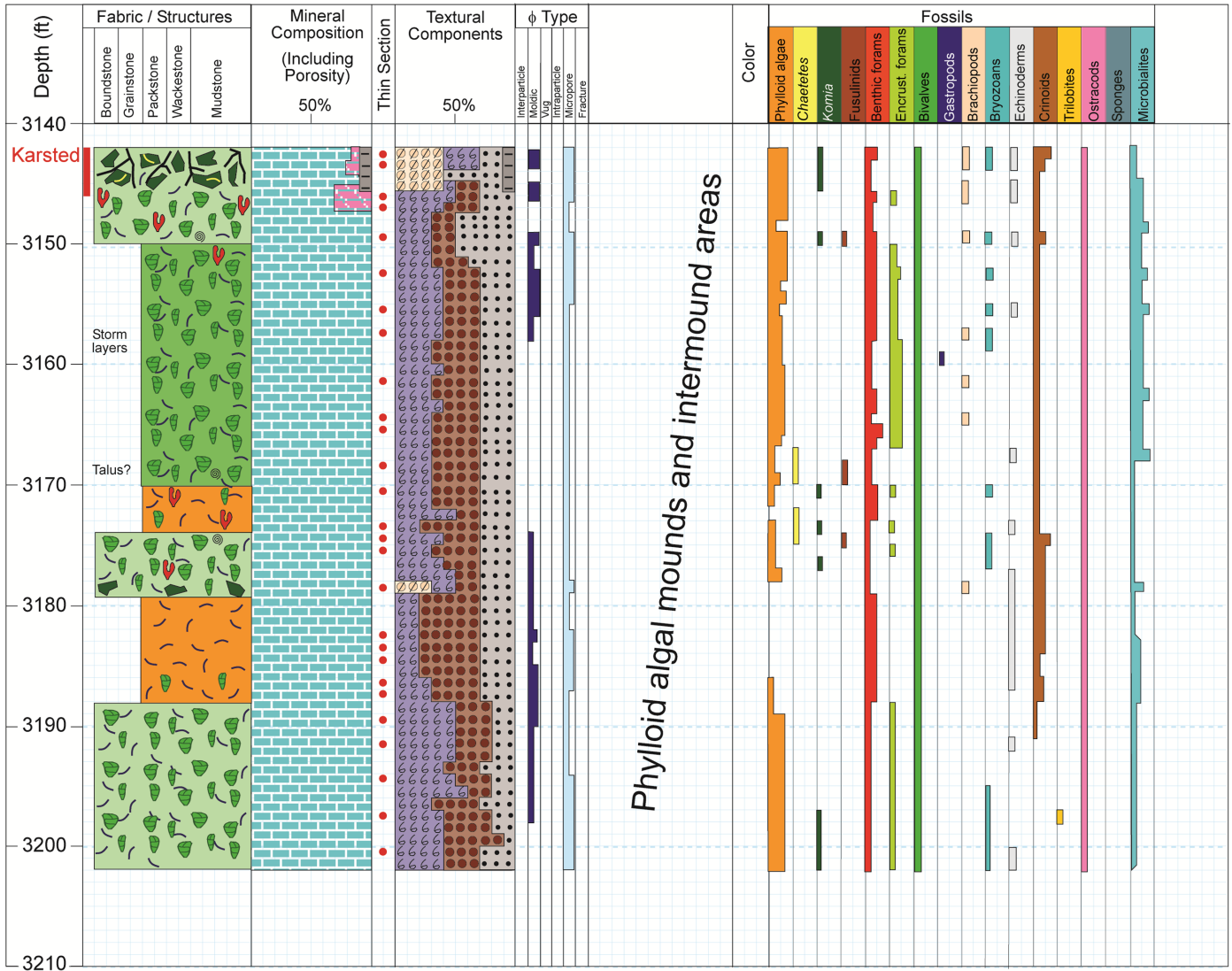


Figure 4. Core description of Sun Oil Caddo Unit Veale Parks No. 36 core.

accelerating voltages (1–10 kV) were generally used on these samples to prevent beam damage, and working distances were 3 to 7 mm. Two types of samples were viewed with the FESEM: polished thin sections and Ar-ion milled samples. Polished thin sections were used to quantify shape, abundance, and distribution of the microrhombic calcite and associated micropores. Ar-ion milled samples (see Loucks et al., 2009, for discussion of de-

scription and preparation of Ar-ion milled samples) are excellent for observing a flat surface without any irregularities related to differential hardness. These samples also allow three-dimensional viewing because they are not impregnated with epoxy. Porosity and permeability measurements were collected on 69 core plugs (1 inch diameter) by Weatherford Laboratory, which also conducted four mercury injection capillary pressure

(MICP) analyses. Two source rock analyses (Leco TOC, Rock-Eval-2, and maturity testing) were completed by GeoMark Petroleum Services Division.

## REGIONAL SETTING, LITHOFACIES, AND DEPOSITIONAL ENVIRONMENT

### Regional Setting

The Pennsylvanian (early Desmoinesian) Caddo Limestone in north-central Texas is up to 800 ft thick (Forehand, 1991) where the uppermost section contains abundant phylloid algal and *Komia* mound complexes. These complexes were deposited on the eastern flank of the Concho Platform (Fig. 5) during the early Desmoinesian (Fig. 2), an age that is based on paleontological data (Turner, 1957). This area was strongly affected by the downwarping of the foreland Fort Worth Basin related to the northwest migration of the Ouachita Thrust Belt (Fig. 5). In addition, the Pennsylvanian sediments were deposited during ice-house conditions that produced rapid and large changes in sea level (e.g., Heckel, 1986). The combined effects of tectonic activity and relative sea-level changes produced well-defined cycles of deposition. In the study area, three cycles of phylloid algal mound deposition (Fig. 6) have been described by several authors (e.g., Miller, 2001). Overlying the upper Caddo karsted surface are the Strawn siliciclastics.

### Lithofacies Review

Several studies have described the lithofacies associated with the Caddo phylloid algal mound complexes as well as the interpreted buildup history (e.g., Lewis, 1987; Forehand, 1991; Weber, 1995; Miller, 2001; Entzminger et al., 2012). Because this present study emphasizes pore networks and not lithofacies, only a few cores are described here (Figs. 3 and 4). The following Caddo lithofacies review is based on the lithofacies descriptions of previous authors, particularly Miller (2001), but the textures of some lithofacies were reinterpreted for the present study. It should be noted that many of the wackestones described by Miller (2001) are actually packstones when the distinct peloids seen in thin section are taken into consideration. These closely packed peloids produce a grain-supported framework. A depositional model is presented in Figure 7 and photographs of core slabs and thin sections showing textures, fabrics, and allochems are presented in Figures 8–15.

### Sponge-Spiculite Wackestone to Packstone Lithofacies (Figs. 7 and 8G–8I)

The lithofacies is dominated by sponge spicules with few to abundant other allochems. Burrows and rare ripples are present. It is rich in carbonate mud and contains some organic matter. Total organic carbon from two Rock-Eval analyses are 0.16%

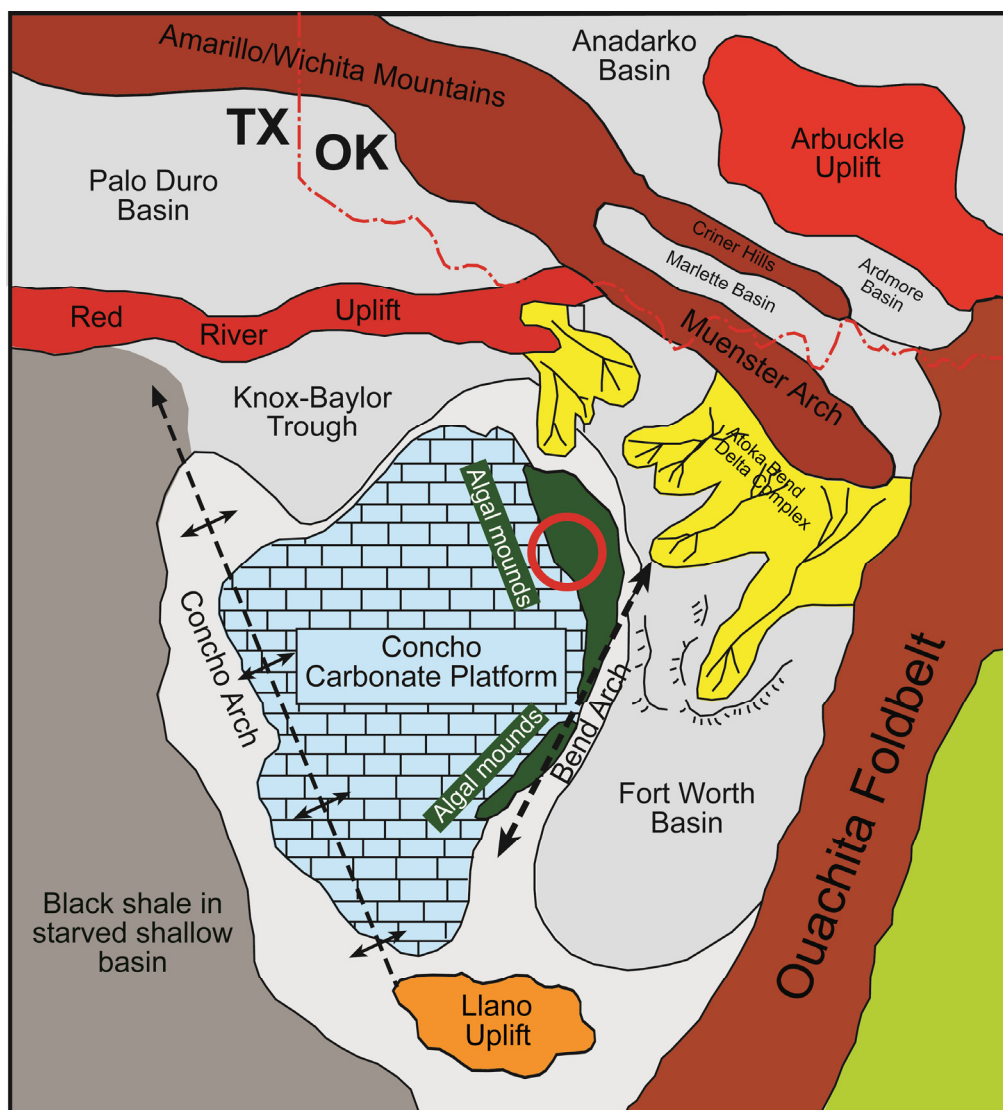


Figure 5. Paleogeographic map of Desmoinesian showing area of this study (modified after Miller, 2001, who modified figure after Cleaves, 2000).

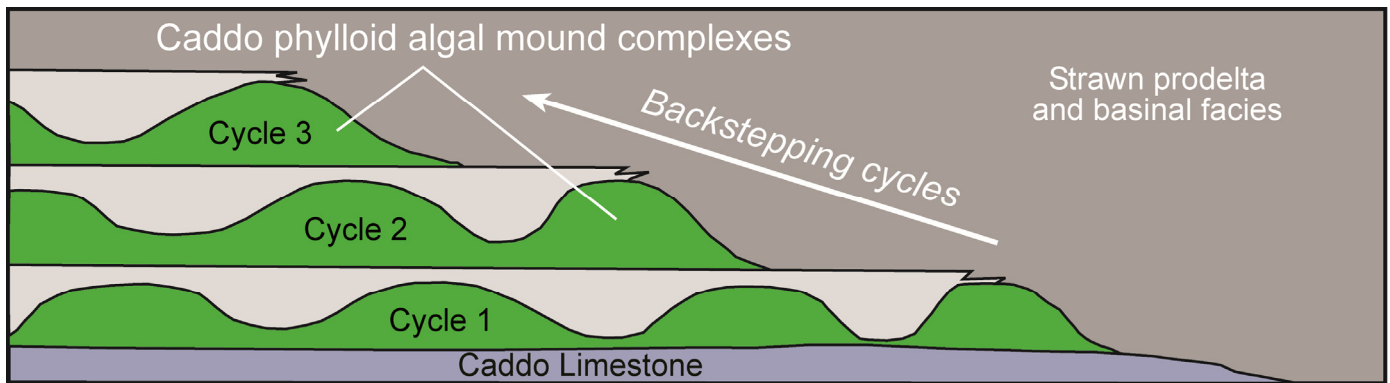


Figure 6. Schematic illustration of three back-stepping phylloid algal mound complexes away from platform edge.

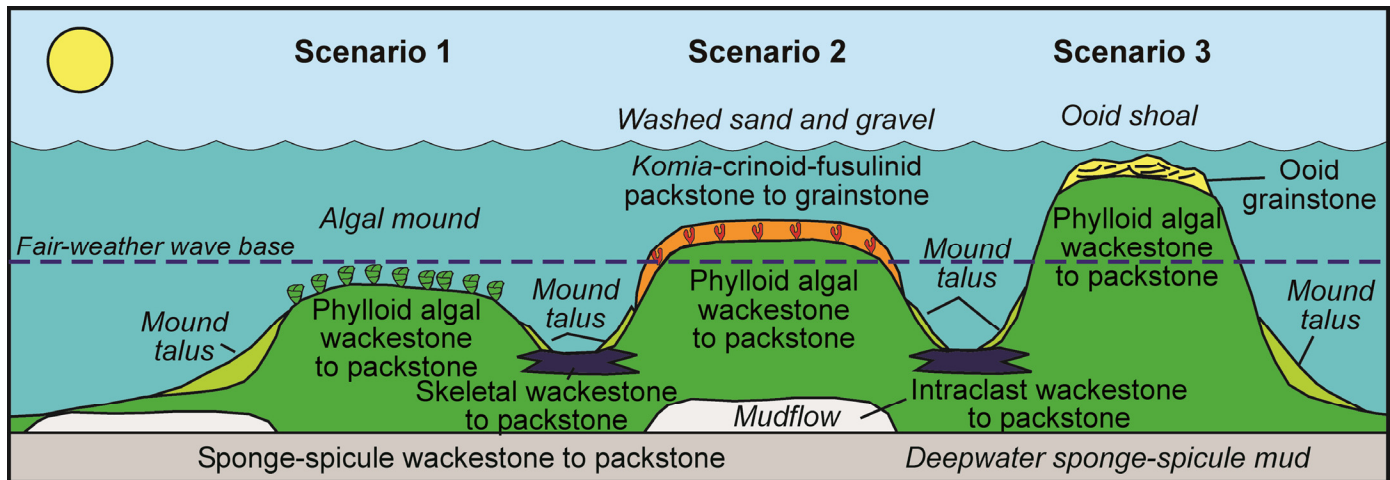


Figure 7. Depositional model of Caddo phylloid algal mound complexes. Two-dimensional model shows different scenarios for mound development. Scenario 1 shows development of phylloid algal mound below fair-weather wave base. Scenario 2 shows *Komia* sand flat formed above fair-weather wave base at top of phylloid algal mound. Scenario 3 shows ooid shoal development over phylloid algal mound. Relief on schematic mounds is vertically exaggerated.

and 0.57%. Various amounts of bryozoan, crinoid, trilobite, and foraminifera fragments are present and interpreted to be transported into the area of sponge-spicule deposition by gravity-flow events.

#### Fusulinid-Crinoid-*Komia* Packstone to Grainstone Lithofacies (Figs. 7, 9A, and 9B)

The packstones range from mud poor to mud rich, whereas the grainstone completely lacks lime mud. Fusulinids, crinoids, and *Komia* grains are the predominant constituents. Other allochems include brachiopods, gastropods, bryozoans, ostracods, phylloid algal fragments, and small benthic foraminifera. The lithofacies is poorly sorted and shows bimodal grain-size distribution through segregation of different grain sizes by layers.

#### *Komia* Wackestones to Grainstone Lithofacies (Figs. 7 and 9C–9E)

*Komia* fragments are the dominant allochem; associated allochems are derived from echinoderms, bryozoans, foraminifera, brachiopods, phylloid algae, ostracods, and possibly mollusks. *Komia* fragments are commonly millimeter-scaled in size (longitudinal axis) and may be encrusted by *Archaeolithophyllum*. The *Komia* thallus is cylindrical and bifurcated, and consists of a thin, central axis of flaring bundles of elongate cells

surrounded by a cortex of concentric layers of subquadratic to rectangular cells (or chambers). The microstructure is well preserved in many samples. Some *Komia* show evidence of minor abrasion; others display intense dissolution and may have been completely dissolved, leaving only molds.

#### Phylloid Algal Bafflestone (Packstone) Lithofacies (Figs. 7, 8A–D, and 9F–J)

Phylloid algae, which dominate this mud-rich facies, acted as an effective baffle to waves and currents, and allowed fine-grain mud particles and peloids to be baffled and trapped. As noted elsewhere in the present study, much of the lime mud is composed of small peloids, some of which are interpreted to be related to cyanobacteria (microbial) precipitation. The phylloid plates range from whole pieces to broken chips. This facies contains lesser amounts of echinoderm and *Komia* fragments. The lithofacies also contains tubular and encrusting foraminifera coating algal plates (Figs. 8C, 9I, and 10A), bryozoans, and ostracods. The algal blades had some rigidity according to Miller (2001), as indicated by the ability of the plates to create sheltered pore space. Also, our observations suggest that the mounds had abundant microbial encrustation and early cement consisting of fibrous aragonite (Figs. 10A, 11E, and 13C) and peloidal Mg-calcite (Figs. 12A, 12C, and 14A). The cavities within the rigid framework contain geopetal sediment fill (Figs. 9J and 14).

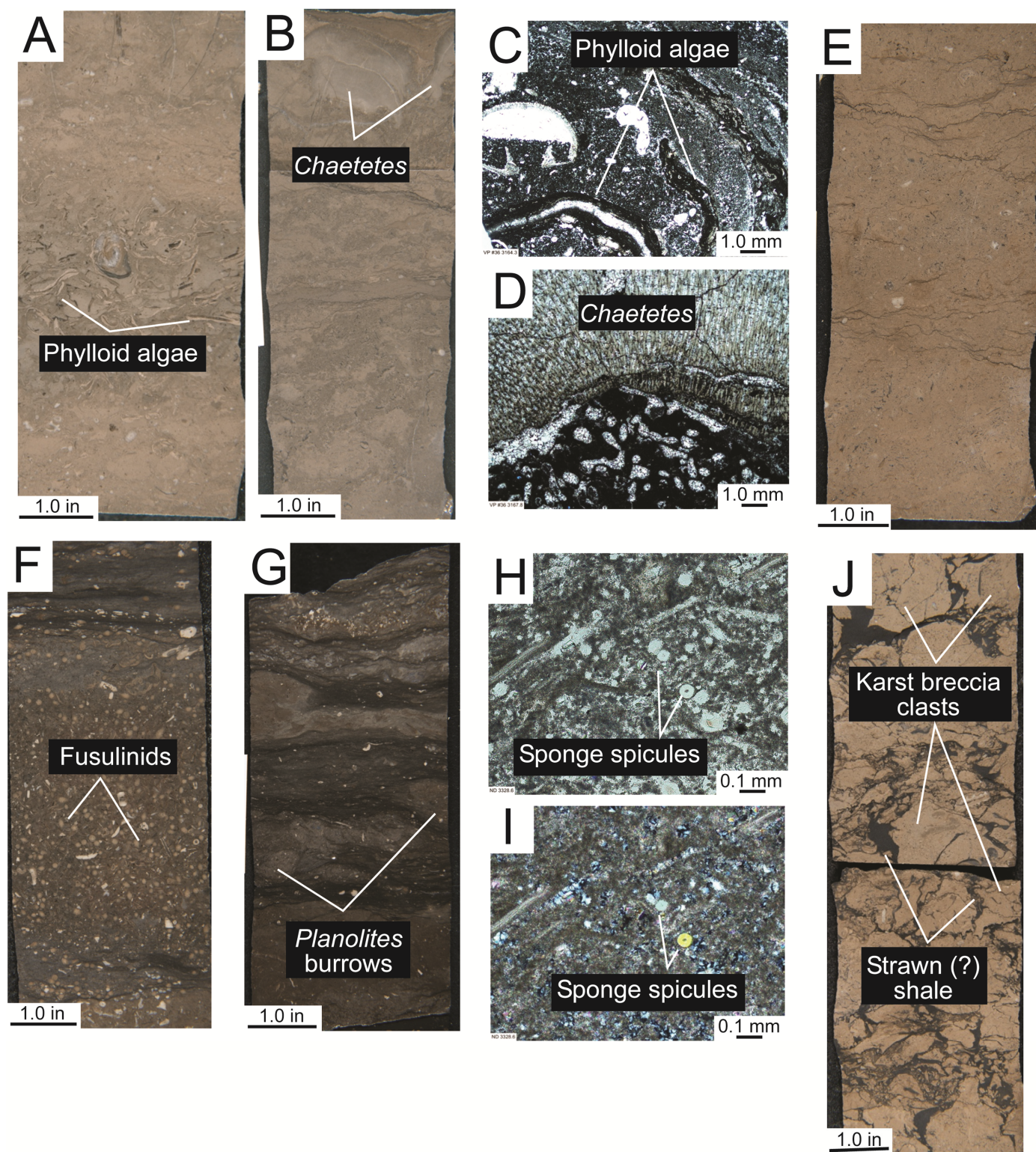


Figure 8. Examples of lithofacies. (A) Veale Parks No. 36, 3168 ft: Burrowed phylloid algal packstone. Algal blades are coated with osagiid encrustations. (B) Veale Parks No. 36, 3167 ft: Burrowed phylloid packstone. Contains large piece of *Chaetetes*. (C) Veale Parks No. 36, 3164.3 ft: Algal blades are encrusted with osagiid encrustations in phylloid algal packstone. (D) Veale Parks No. 36, 3167.8 ft: *Chaetetes* fragment and cyanobacteria in phylloid algal packstone. (E) Veale Parks No. 36, 3167.8 ft: Peloidal skeletal packstone. (F) Newell Dell No. WI-2, 3327 ft: Debris flow of fusulinid and *Komia* grain-dominated packstone overlain by deepwater argillaceous mudstone. (G) Newell Dell No. WI-2, 3324 ft: Sponge-spicule-rich skeletal wackestone. (H) Newell Dell No. WI-2, 3328.6 ft: Sponge-spicule-rich skeletal wackestone in plane light. (I) Same thin section as H but under polarized light. (J) Veale Parks No. 36, 3144 ft: Karst breccia with matrix of Strawn black mudstone.

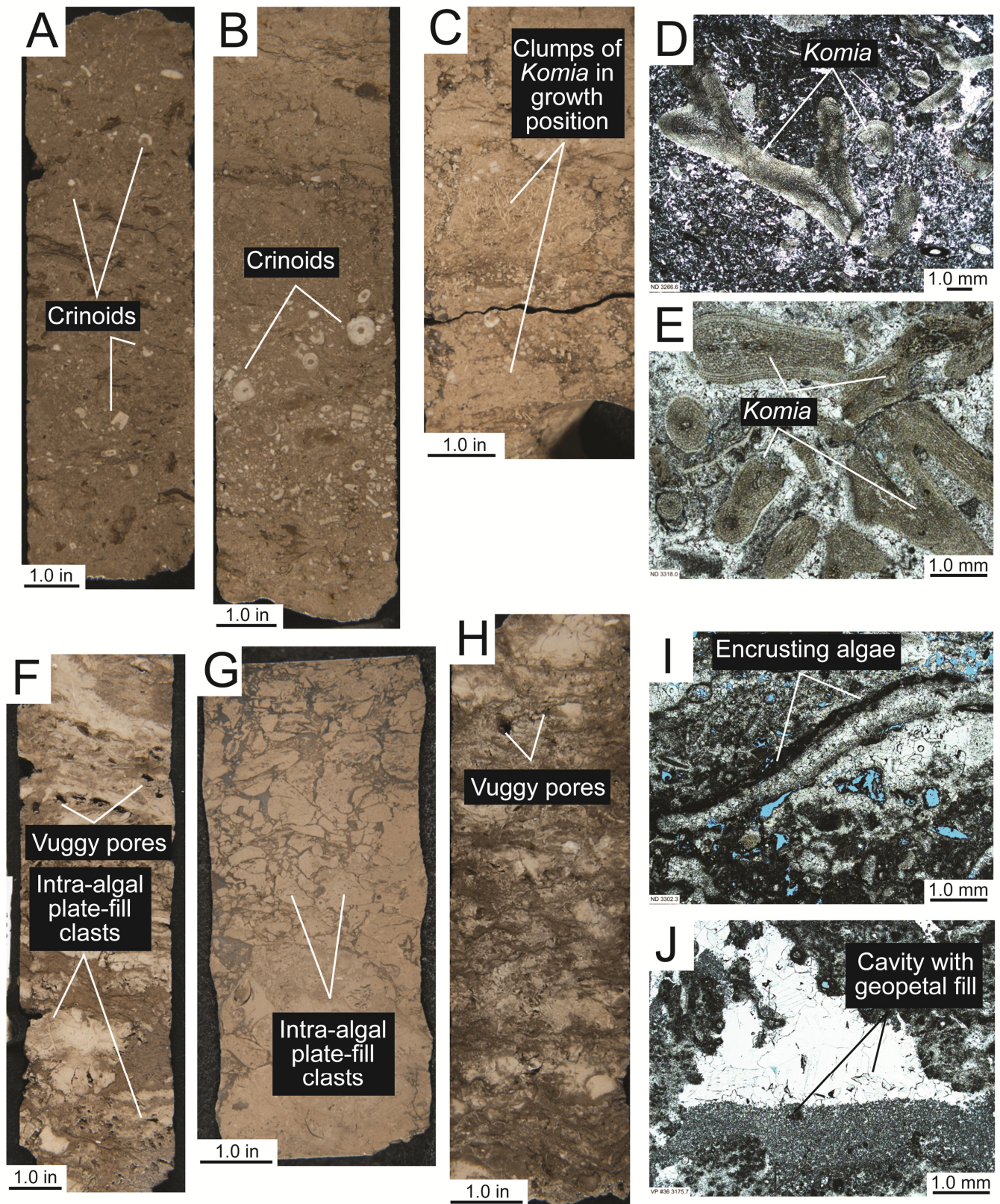


Figure 9. Examples of lithofacies. (A) Newell Dell No. WI-2, 3278 ft: Burrowed crinoid-*Komia* lime packstone. (B) Newell Dell No. WI-2, 3272 ft: Burrowed crinoid-*Komia* lime packstone. Crinoids may be concentrated by storm deposits. (C) Newell Dell No. WI-2, 3288 ft: Karsted crinoid-*Komia* lime packstone. Black seams are former open areas between karsted clasts now filled with Strawn black mudstone. Several clasts contain clumps of *Komia* in growth position. (D) Newell Dell No. WI-2, 3266.6 ft: Intact fragment of *Komia*. (E) Newell Dell No. WI-2, 3218 ft: Fragments of *Komia*. (F) Newell Dell No. WI-2, 3286 ft: Phylloid algal bafflestone. Clasts are mud-fill between dissolved algal blades. Contains vuggy pores. (G) Veale Parks No. 36, 3146 ft: Phylloid algal bafflestone. Clasts are mud-fill between dissolved algal blades. (H) Newell Dell No. WI-2, 3309 ft: Phylloid algal bafflestone. Contains vuggy pores. (I) Newell Dell No. WI-2, 3302.3 ft: Phylloid algal bafflestone with interparticle pore created by collapse of algal molds. (J) Veale Parks No. 36, 3146 ft: Phylloid algal bafflestone. Geopetal fill in algal sheltered cavity.

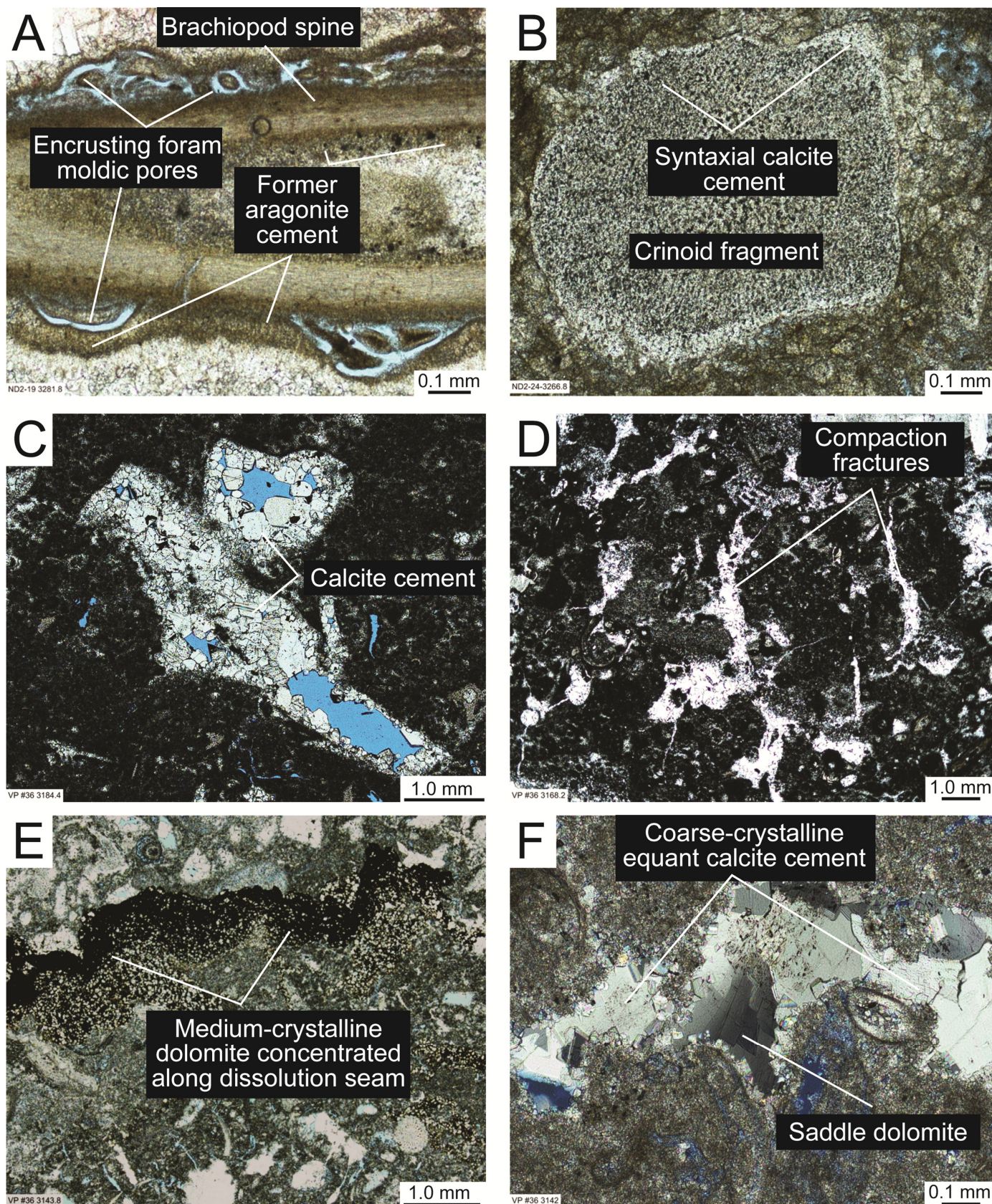


Figure 10. Examples of diagenesis. (A) Brachiopod spine with encrusting foraminifera by fibrous aragonite cement. Encrusting foraminifera dissolved to form moldic pores. (B) Syntaxial calcite cement on crinoid fragment. (C) Moldic pores after phylloid algae dissolution. Moldic pores partly filled with fine- to medium-crystalline calcite. (D) Compaction fractures, now filled with calcite, after dissolution and collapse of aragonite phylloid algal plates. (E) Pressure solution seam concentrating medium-crystalline euhedral dolomite. (F) Coarse-crystalline calcite and coarse-crystalline saddle dolomite filled moldic pore. Cross-polarized light.

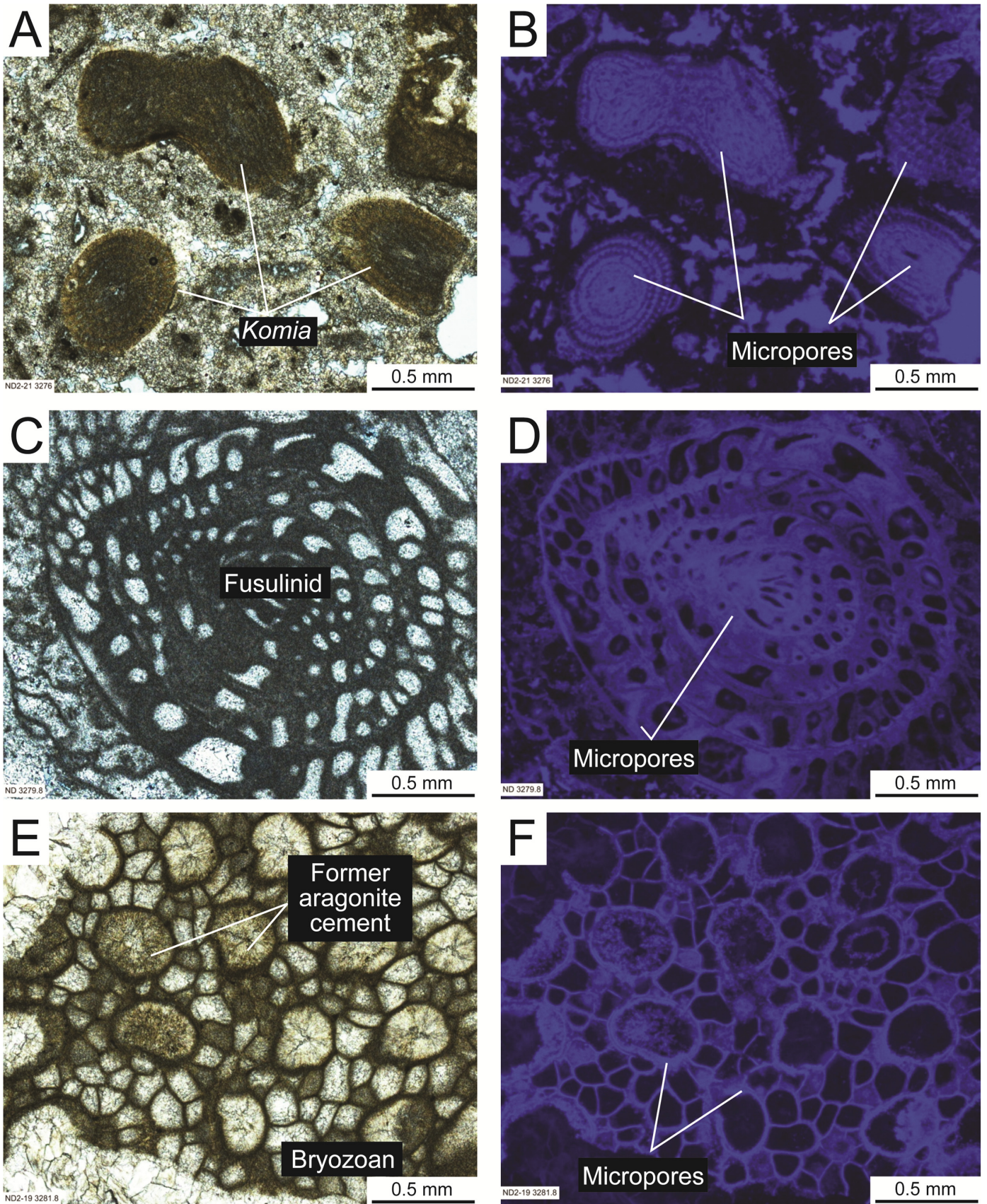


Figure 11. Examples of micropore development. (A) Micropores in *Komia* fragments. (B) UV photomicrograph of A showing micropores in blue. (C) Micropores in fusulinid. (D) UV photomicrograph of C showing micropores in blue. (E) Micropores in bryozoan. (F) UV photomicrograph of E showing micropores in blue.

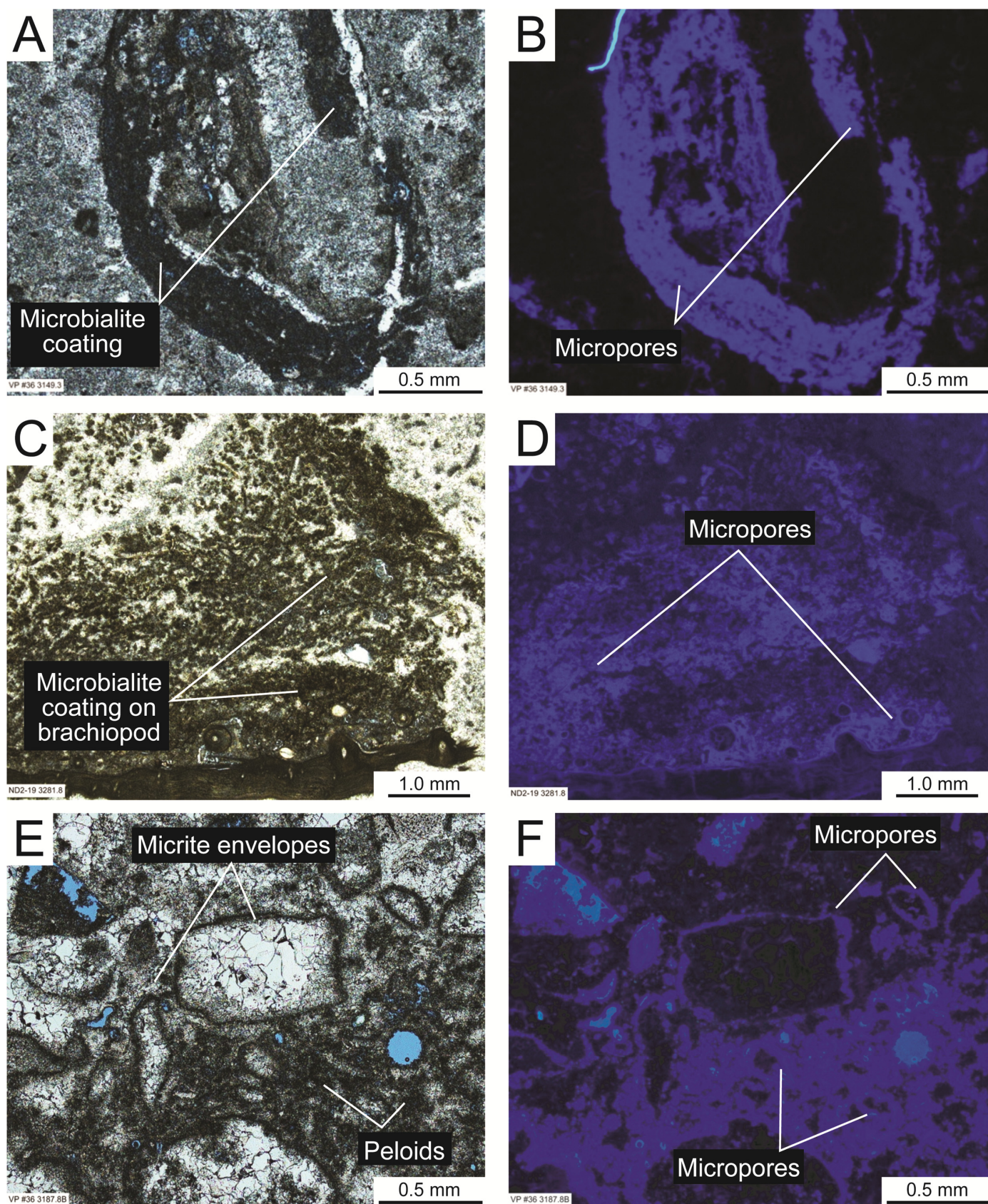


Figure 12. Examples of micropore development. (A) Micropores in microbialite coating. (B) UV photomicrograph of A showing micropores in blue. (C) Micropores in former Mg-calcite peloids related to cyanobacteria. (D) UV photomicrograph of C showing micropores in blue. (E) Micropores in micrite envelopes. (F) UV photomicrograph of E showing micropores in blue.

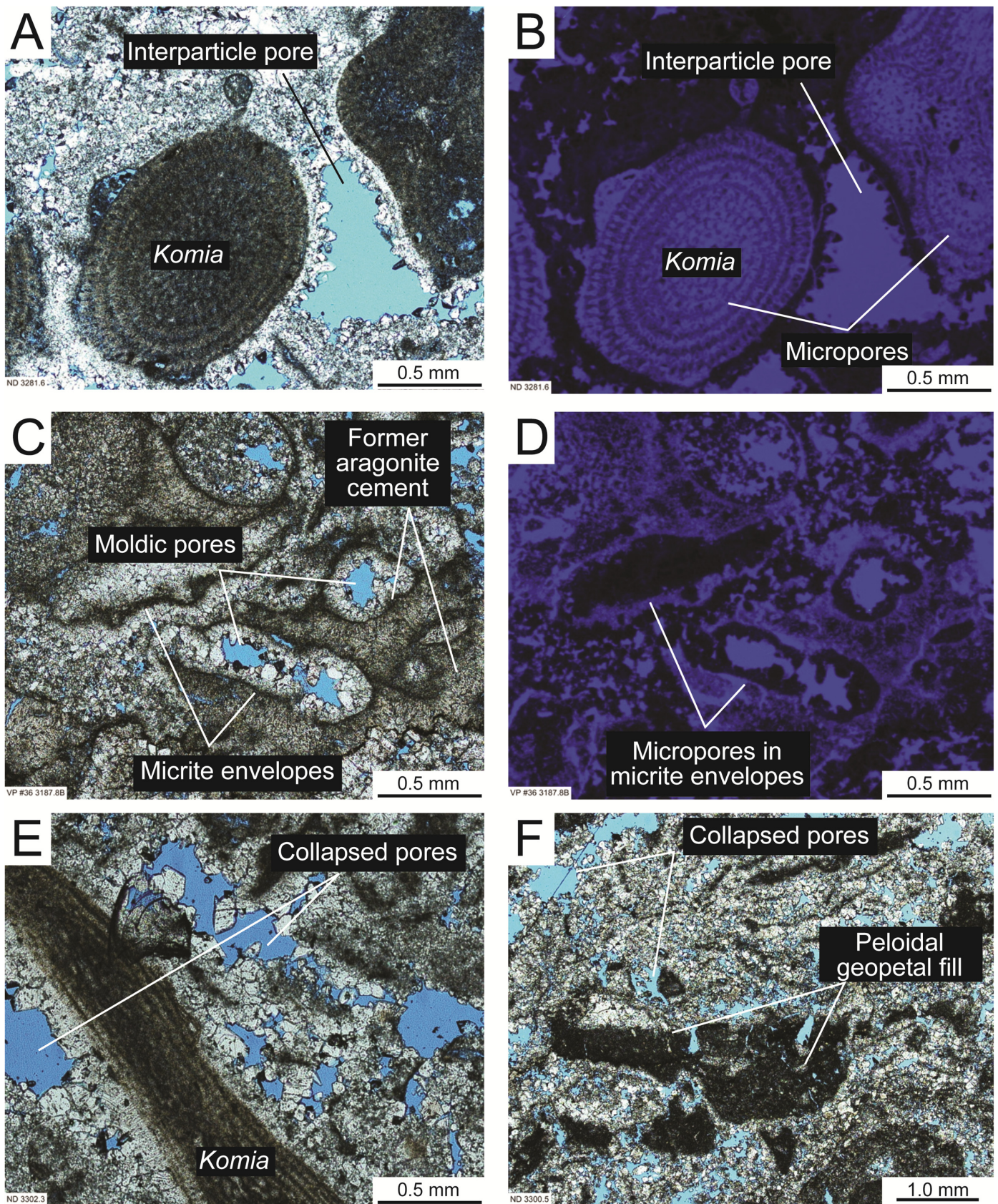
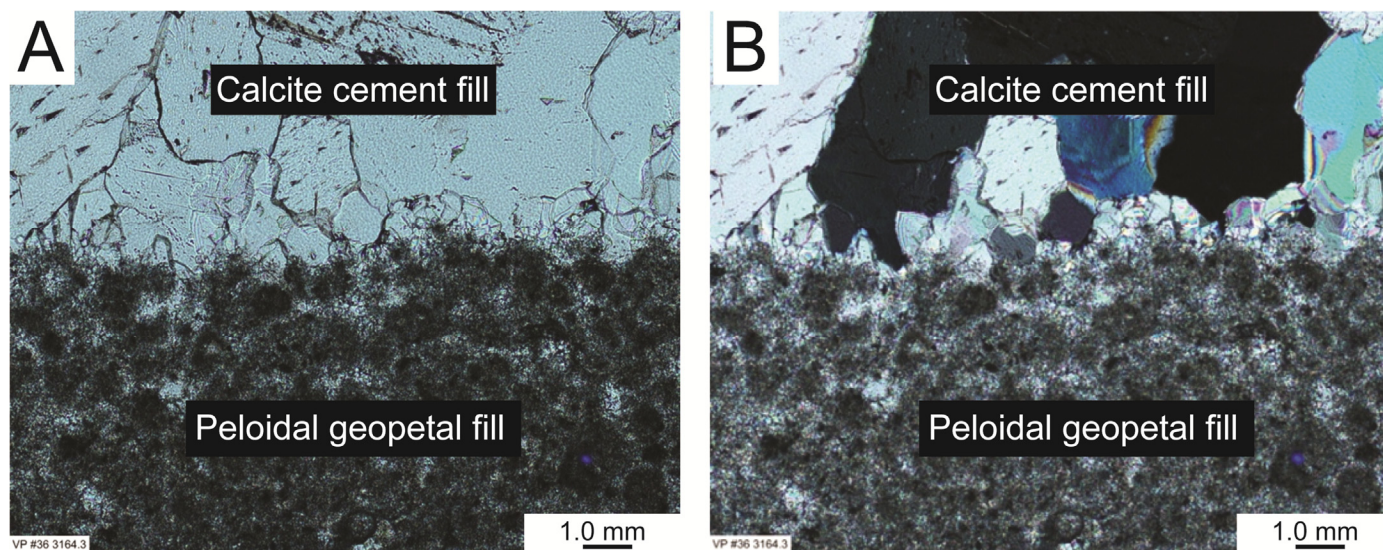


Figure 13. Examples of pore networks emphasizing macropores. (A) Interparticle pore rimmed by fine-crystalline equant to bladed calcite cement. (B) UV photomicrograph of A showing pores in blue. *Komia* allochems are microporous. (C) Moldic pores partly filled by fine-crystalline equant to bladed calcite cement. (D) UV photomicrograph of C showing pores in blue. Many micrite envelopes are microporous. (E) Framework collapse after dissolution of aragonite phylloid algal blades producing vuggy pores. (F) Collapse of phylloid algal framework producing vuggy pores. Relict geopetal fill of peloids remains.



**Figure 14. Geopetal cavity fill.** (A) Geopetal pore fill showing fine peloids interpreted to be precipitated Mg-calcite peloids associated with microbial processes. Remaining pore is filled with fine- to medium-crystalline equant calcite. (B) Photomicrograph of A under cross-polarized light.

#### Skeletal Wackestone to Packstone Lithofacies (Fig. 8E)

A variable mixture of skeletal grains in a lime-mud matrix. Grains include fragments of crinoids, brachiopods, phylloid algae, foraminifera, brachiopods, bryozoans, and *Komia*. Peloids are extremely common and may be the predominant allochem.

#### Clast-Rich Wackestone Lithofacies

This facies contains dark, angular lime-mud clasts in a lighter-shaded lime-mud matrix. The clasts may have been partly lithified according to Miller (2001). Clasts range in size from 0.25 to 13 mm. The matrix mud contains a mixture of skeletal fragments, whereas the lime-mud clasts contain mostly foraminifera. This facies was not encountered in the two cores investigated.

#### Skeletal Ooid Packstone to Grainstone Lithofacies

This lithofacies ranges from a relatively pure ooid grainstone to ooid-rich skeletal grainstone (Miller, 2001). *Komia* and crinoid fragments are the dominant skeletal allochems associated with the ooids. This facies was not encountered in the two cores investigated.

### Cycles

As noted in Figure 6, three cycles of buildups have been defined in the study area (e.g., Miller, 2001). This present study only encountered the uppermost cycle. Within the upper cycle, higher-order cycles can be delineated from the core descriptions (Figs. 3 and 4).

In the Newell Dell No. WI-2 core, two cycles of phylloid algal buildups are noted; in the Veale Parks Caddo Unit No. 36, three cycles appear to have formed. With the limited data available in this investigation, one cannot assign these buildup cycles to short-term sea-level changes or to autocyclicity.

### Depositional Model

A number of authors have proposed deposition models for the development of the phylloid algal buildups in Stephens County (e.g., Lewis, 1987; Forehand, 1991; Weber, 1995; Miller, 2001). More in-depth studies of these mounds in other areas

have been completed by a number of authors (e.g., Wahlman, 2001, 2002). A modified depositional model is proposed in Figure 7 based upon what other authors have noted and our new observations and interpretations. We suggest that the lithofacies are a response to third- or fourth-order sea-level changes. Within an icehouse climatic period, rapid sea-level changes of significant magnitude occur (e.g., Heckel, 1986).

Because the buildups are developed on the higher-relief Concho Platform, the lowstand systems tract is only represented by an exposure surface or unconformity. Miller (2001) recognized exposure surfaces at the top of the cycles. Both cores described have a karsted surface at the top of the Caddo Limestone (Figs. 8J and 9C). The karst breccia clasts have black argillaceous mudstone between them that is interpreted as filtering down from the Strawn siliciclastics above.

The sponge-spiculite lithofacies is the basal unit of the larger cycle (Fig. 7) and is interpreted as the basal facies of the transgressive systems tract (TST). This is a deeper-water facies, and the abundance of sponge spicules and the slightly elevated organic-matter content suggests a dysaerobic setting below storm-wave base. Associated shallower-water allochems were transported into the deeper-water setting by gravity-flow currents. In this deeper-water setting, mud flows were emplaced carrying dark lime-mud clasts and skeletal debris. The source of the mud clasts is not evident but may have been distal, partly lithified mud mounds. Later in the TST, as water depths decreased in response to sediment accumulation and as sea-level rise slowed, phylloid algal mounds began to grow beneath a fair-weather wave base (Fig. 7). Phylloid bafflestones formed the main core of the mound. Entzinger et al. (2012) estimated the mounds to be between 10 and 30 ft high. The mounds have been suggested to coalesce as they grew (Weber, 1995). In the protected, low-energy intermound areas, skeletal muds (wackestone and packstone) accumulated in a low-energy environment (Fig. 7). The biota in this intermound area grew in situ or was transported and included phylloid algae, *Komia*, crinoid and bivalve fragments, benthic foraminifera, and ostracods (Figs. 3 and 4).

Sea-level rise slowed during the sea-level highstand, and continued sedimentation resulted in the deposition of shallower-water facies above a fair-weather wave base. As current and wave energy increased, fusulinid-crinoid-*Komia* sands and gravels (grainstones) and then ooid sands (grainstones) were deposited

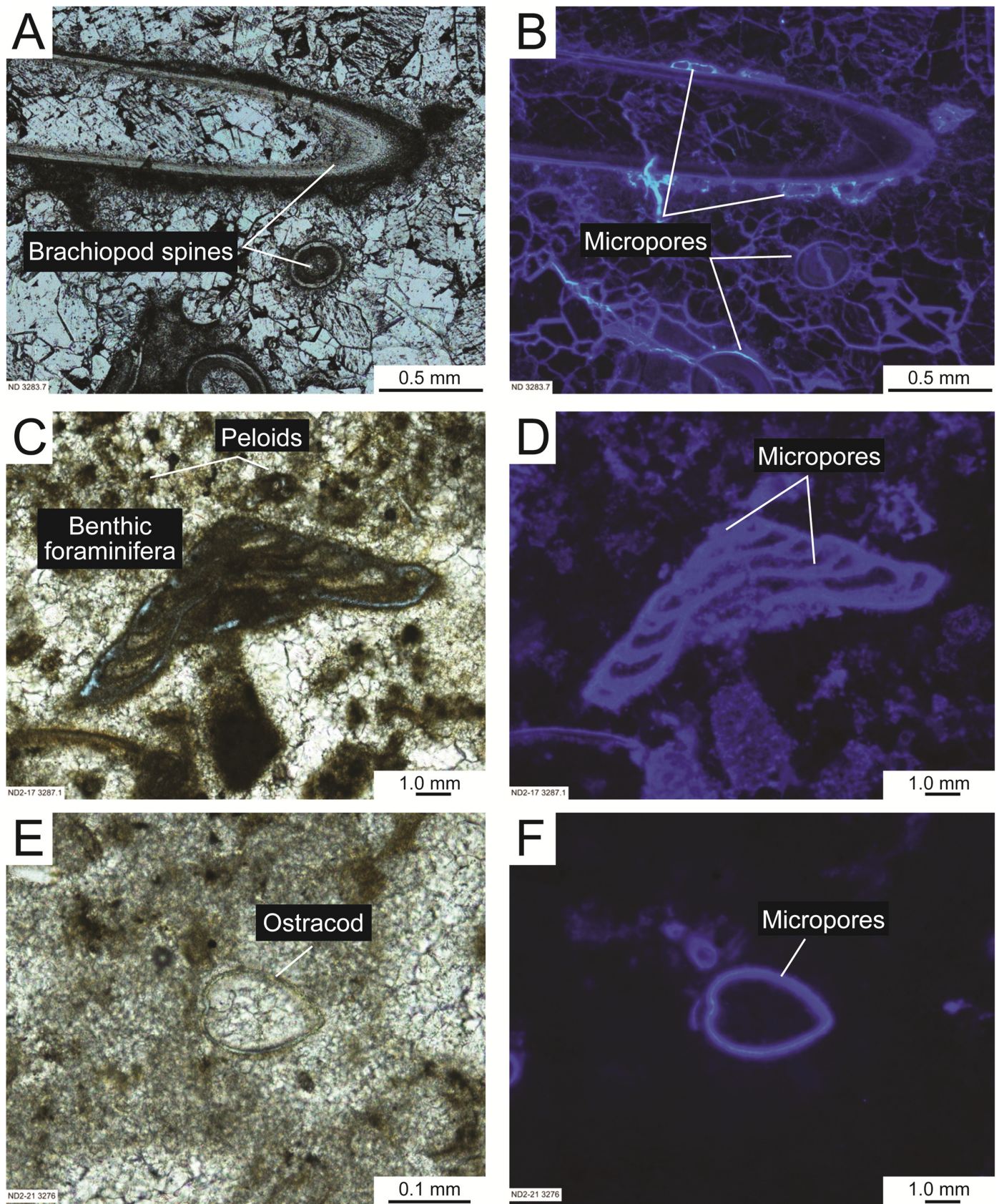


Figure 15. Examples of micropore development. (A) Micropores in encrusting foraminifera and in micrite envelope rimming brachiopod spine. (B) UV photomicrograph of A showing micropores in blue. (C) Micropores in benthic foraminifera. (D) UV photomicrograph of C showing micropores in blue. (E) Micropores in ostracod. (F) UV photomicrograph of E showing micropores in blue.

ed (Fig. 7). The cross-bedded ooids represent the highest energy area in the shoaling complex and are probably associated with topographic paleohighs over the relict algal mounds. The more skeletal-rich ooid grainstones may have been back shoal, fore shoal, or deeper areas between shoals. The fusulinid-crinoid-*Komia* grainstone also represent higher-energy conditions, but not as high energy as the ooid grainstone. These biotrital accumulations of Wahlman (2001, 2002) are interpreted as having formed on skeletal sand flats that were well washed by currents.

## DIAGENESIS AND PORE-NETWORK DESCRIPTION

### Paragenesis

To understand the origin of the macro- and micropores, their formation relative to other diagenetic features must be established. Figure 16 is a paragenesis diagram showing the different diagenetic stages and interpreted diagenetic environments for all diagenetic features seen in the Caddo cores. The pore-network evolution is also shown at the bottom of the diagram.

The general diagenetic environments include: (1) marine, (2) meteoric, (3) shallow burial, and (4) deeper burial. Each major stage of diagenesis had a significant effect on pore development, preservation, or destruction.

### Marine Diagenetic Environment

Fibrous isopachous aragonite (now calcite) cement rims (Figs. 10A and 11E) precipitated around grains within interparticle and intraparticle pores. This cement is common within the phylloid algal lithofacies. Micrite rims or envelopes (Figs. 12E and 13C) formed around grains and on aragonite cement rims by algal and fungi borings that precipitated Mg-calcite-rich layers (Winland, 1968), which commonly transform to microrhombic calcite with associated micropores (Loucks et al., 2013). Mechanical abrasion by bioturbation, currents, and waves fragmented grains (Fig. 13C), thereby reducing intraparticle pores. Microbialite colonies grew on grains (Figs. 12A and 12C) and may have bound some grains together. Many of the abundant fine peloids are interpreted to be microbial in origin and thus are thought to have been originally Mg-calcite. Peloidal cement formed in cavities and in association with microbialites (Fig. 14). Other peloids are probably fecal pellets or a product of marine snow.

### Meteoric Diagenetic Environment

During exposure of parts of the Caddo unit, meteoric waters caused dissolution of aragonite grains, creating moldic pores (Figs. 10C and 13C). This exposure is evidenced by a well-developed karsted surface at the top of the Caddo section. Fine- to medium-equant calcite precipitated, sourced primarily from aragonite dissolution, initiating a rigid framework and filling some interparticle and intraparticle pores (Figs. 10C, 11A, 12E, 13A, 13C, 13E, and 15A–15C). Syntaxial calcite cement precipitated around echinoid ossicles occluding some interparticle pores (Fig. 10B). Many of the Mg-calcite allochems, peloids, mud, and micrite rims transformed to micropolyhedral calcite with associated micropores (Figs. 17–20). The process of Mg-calcite transforming to microcrystalline calcite has been reviewed by Loucks et al. (2013).

### Shallow-Burial Diagenetic Environment

Micropolyhedral calcite related to the stabilization of Mg-calcite continued to grow in this diagenetic environment. Additional medium-crystalline calcite cement continued to precipitate and occluded macropores. Megaquartz replaced fibrous brachiopod shells and fusulinid tests. Coarse-crystalline equant calcite

started to precipitate and continued into the deeper burial realm (Figs. 10F and 14). This cement tended to occlude many of the macropores.

### Deeper-Burial Diagenetic Environment

Coarse-crystalline equant calcite continued to precipitate and occluded more macropores. Saddle dolomite precipitated and also filled in macropore space (Fig. 10F). Collapse of some large moldic pores associated with the dissolution of large aragonite phylloid algae produced vugs and compaction fractures (Fig. 10D). Stylolites and pressure solution seams were initiated (Fig. 10E). Medium-crystalline euhedral dolomite (Fig. 10E) precipitated in close association with pressure solution seams.

### Pore Network

The pore network in the Caddo Limestone consists of both macro- and micropores (Fig. 13). Macropores (>10  $\mu\text{m}$  in diameter), pores that contribute to the higher-quality reservoirs, include interparticle, intraparticle, and moldic pores (Fig. 13). Interparticle pores are the original pores between grains. Some are reduced by depositional lime mud and equant calcite cement. Intraparticle pores lie within skeletal grains; many are partly to totally occluded by calcite cement. Moldic pores are the product of the dissolution of aragonite allochems such as phylloid algae and mollusks.

Micropores (<10  $\mu\text{m}$  in diameter) formed in former Mg-calcite allochems (Figs. 11, 13A, 13B, and 15), micrite rims (Figs. 13C and 13D), and microbialites and their associated peloids (Figs. 12A–12D). Structureless (nonpeloidal) lime mud is rarely microporous. A wide array of former Mg-calcite allochems show well-developed micropores including *Komia*, fusulinid, bryozoans, ostracods, encrusting foraminifera, benthic foraminifera, and brachiopod shells and spines (Figs. 11, 12, and 15). Microbialite coatings also show well-developed micropores (Figs. 12A–12D), as well as numerous associated small peloids (interpreted to be related to microbialites) (Figs. 12E and 12F). Patches, clots, and clasts of mud—which are microporous—may also be related to microbialites. Micrite rims are abundant and contain micropores (Figs. 12E, 12F, 13C, and 13D).

### Micropore Origin and Characterization

As previously stated, the origin of micropores in the Caddo Limestone is related to the transformation of Mg-calcite allochems, peloidal muds, and micrite envelopes to microcrystalline calcite, as described by Loucks et al. (2013). The micropore system in the Caddo Limestone was characterized by analyzing thin sections, mercury injection capillary pressure (MICP) data, and four Ar-ion milled samples with a FESEM. Figures 17–20 present FESEM photomicrographs of the pores and pore networks.

The micropores occur between micropolyhedral calcite crystals (Figs. 17–20) that predominately range in crystal size between 2 and 3  $\mu\text{m}$ . However, some crystals are as large as 5  $\mu\text{m}$ , and some are less than 1  $\mu\text{m}$ . The crystal shape is polyhedral (Figs. 18C, 18D, 18F, and 20D) instead of the common simple rhombohedron, as seen in many other occurrences of microporous carbonates. The shape appears to be a combination of scalenohedron and rhombohedron crystal morphologies. For a detailed discussion on shapes of microcrystalline calcite with micropores, see Kaczmarek et al. (2015).

Some areas that appear to be larger crystals are actually composed of coalesced microcrystals (Figs. 17F, 18B, 18C, and 19C–19F). The microcrystals are evidenced by the triangular-shaped nano- to micropores between them. Without high-resolution FESEM analysis, these micropolyhedral crystals would be misinterpreted as very fine- to fine-crystalline calcite, not the coalescing of microcrystals of calcite.

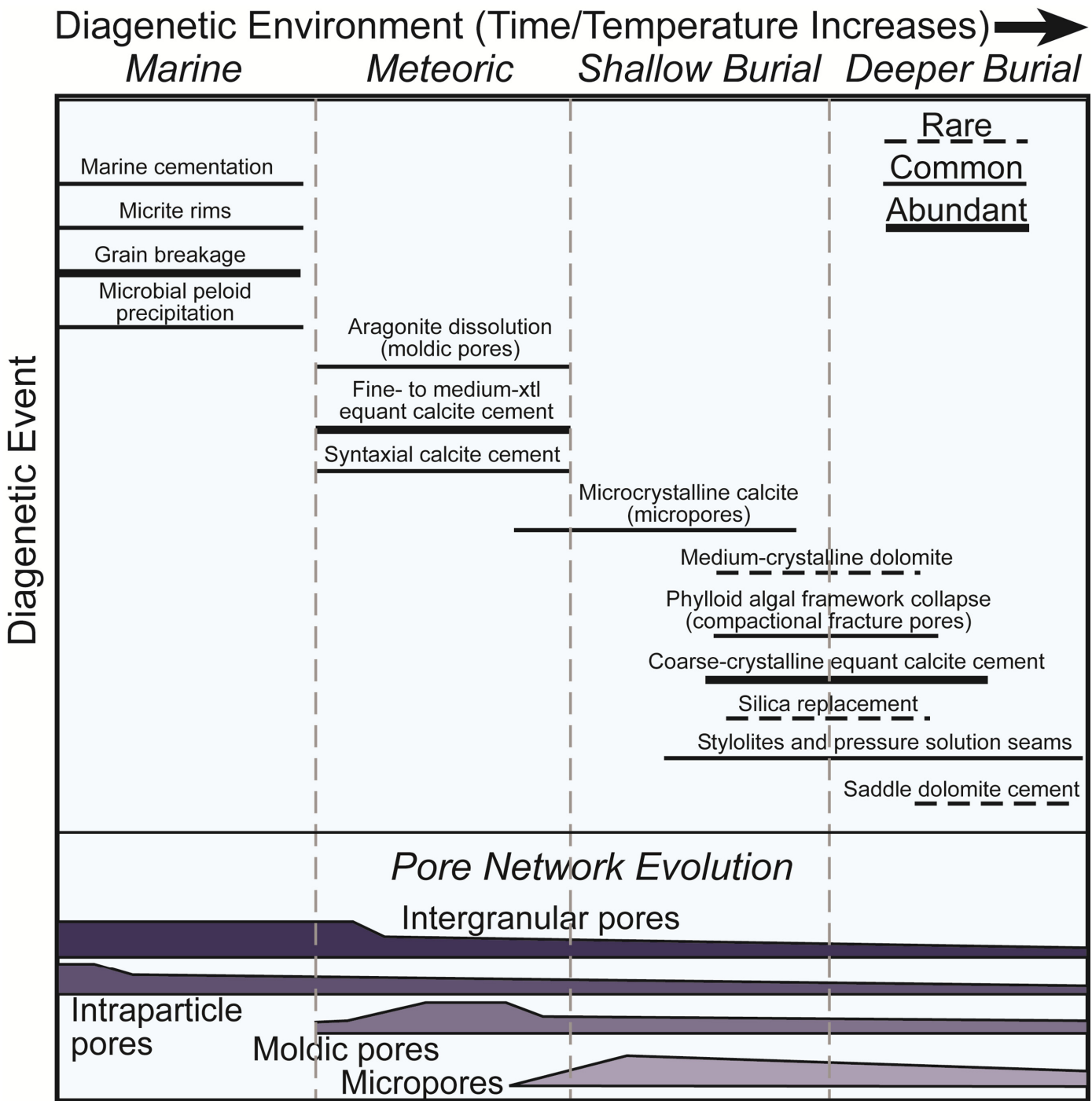


Figure 16. Paragenesis of Caddo lithofacies. General pore network evolution shown at bottom.

Because of the friability of micropore areas, it is difficult to measure pore sizes between micropolyhedral crystals with confidence. We believe that during sample preparation, some micropolyhedral crystals were plucked. Our best estimation of micropore sizes is from ~100 nm to 10 μm.

Many of the microporous areas are confined to individual allochems such as *Komia* skeletons (Figs. 11A, 11B, and 17C–17F). In some sample patches, micropores appear to be connected to the effective pore system by pores ranging in diameter from several microns to 30 μm (e.g., Figs. 17A, 17B, 18B, 18E, and 20C). In thin section, larger pores—the major contributors to hydrocarbon flow—are visible (Fig. 13). The interparticle pores are up to 800 μm in diameter, and the moldic pores are up to 1 mm. The larger collapsed vuggy pores in the phylloid algal

packstones are associated with some of the better permeability, according to Weber (1995) (Figs. 9F, 9H, 13E, and 13F).

### RESERVOIR QUALITY

Porosity and permeability were measured on 69 core plugs by Weatherford Labs. The results show a wide range of porosity and permeability (Fig. 21). Porosity ranges between 0.8% and 25.1%, and permeability ranges between 0.01 md and 370.5 md. Mean porosity is 9.04%, and geometric mean permeability is 0.74 md. Based on lab analyses of 386 samples from the Caddo Limestone in Parks Field (Stephens County), Entzminger (2012) reported that mean porosity is 5.2% and geometric mean permeability is 0.42 md.

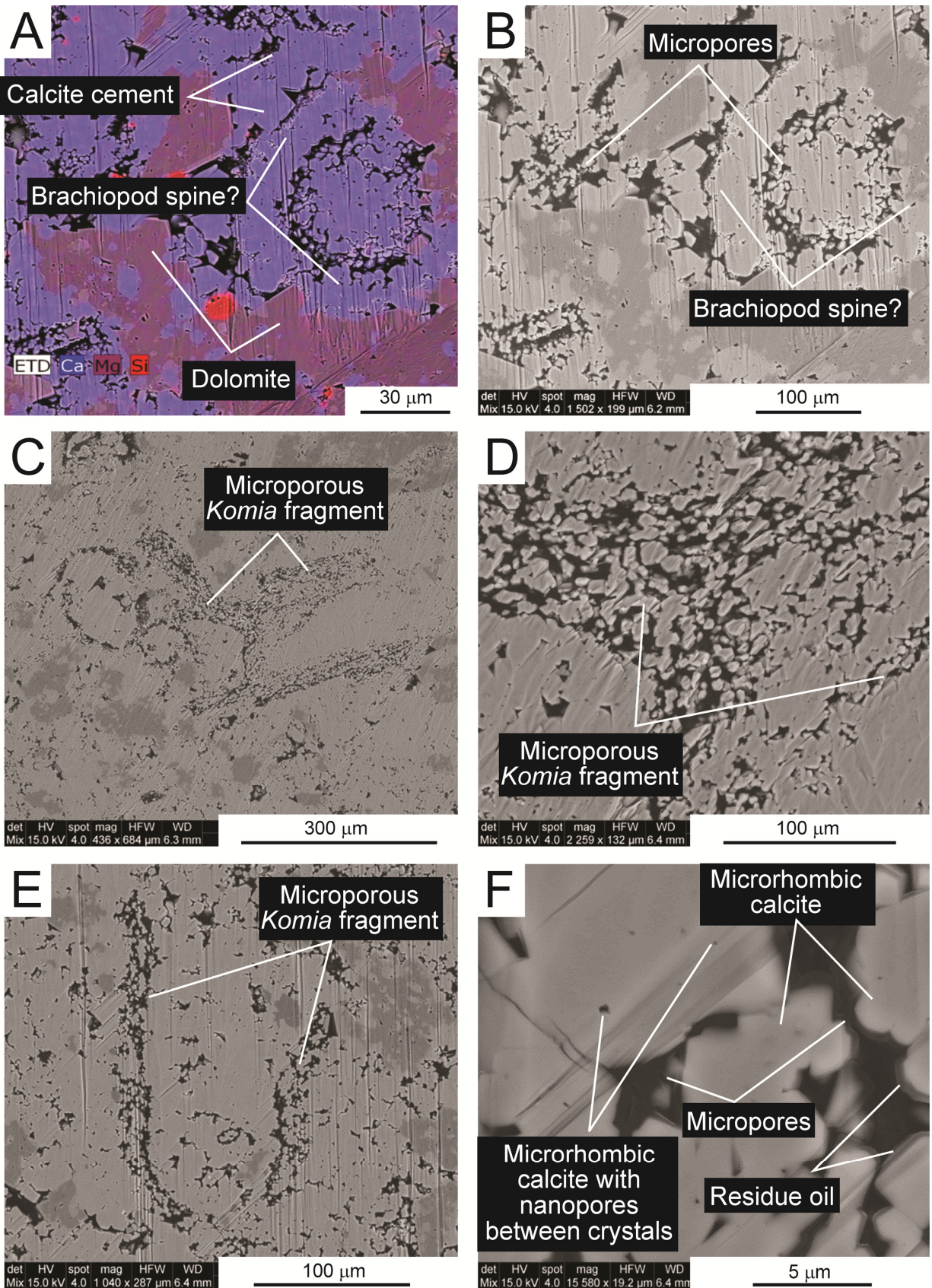


Figure 17. Examples of micropore development as shown by FESEM Ar-ion milled sample 3267 ft. (A) FESEM photograph overlain by energy dispersive spectrometry (EDAX) elemental map. Sample is calcite with some dolomite. (B) Sample showing both macro- and micropores. Circular allochem may be cross section of brachiopod spine. (C) *Komia* fragment with micropores. (D) Close-up of C showing microrhomboidal calcite. (E) *Komia* fragment with micropores. (F) Close-up of E showing microrhomboidal calcite and associated micropores. Larger grains are actually coalesced microrhombic calcite crystals with nanopores in between. Residue oil coats some crystals.

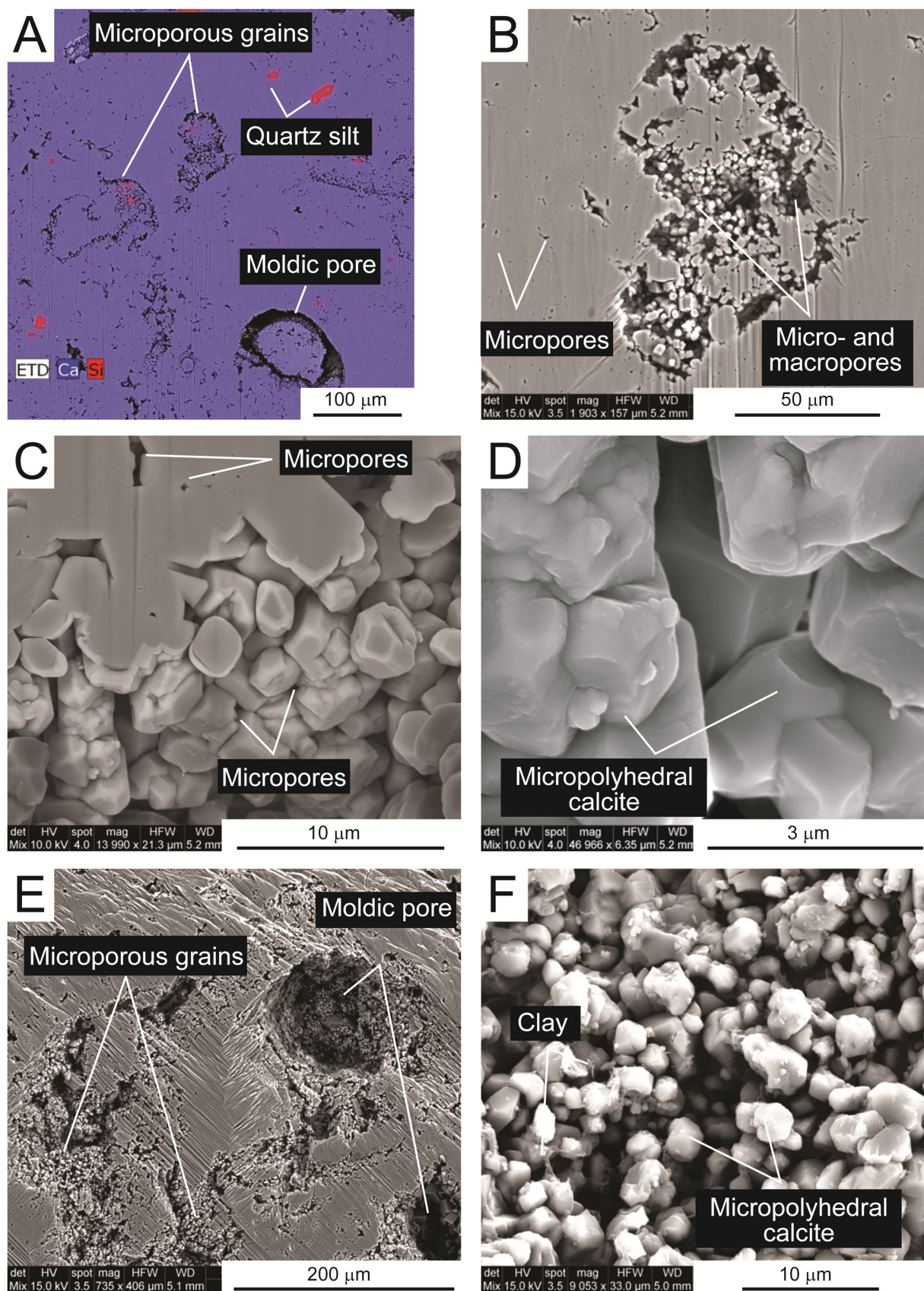


Figure 18. Examples of micropore development as shown by FESEM Ar-ion milled sample 3142.7 ft. (A) FESEM photograph overlain by EDAX elemental map. Sample is calcite with rare quartz silt and clay. (B) Former Mg-calcite grain now composed of micropolyhedral calcite and associated micropores. Some micropolyhedral calcite may have been removed by sample preparation. (C) Close-up of B showing micropolyhedral calcite and associated micropores. (D) Close-up of C showing micropolyhedral calcite. (E) Former Mg-calcite grain that transformed to micropolyhedral calcite and associated micropores. (F) Close-up of E showing micropolyhedral calcite and associate micropores.

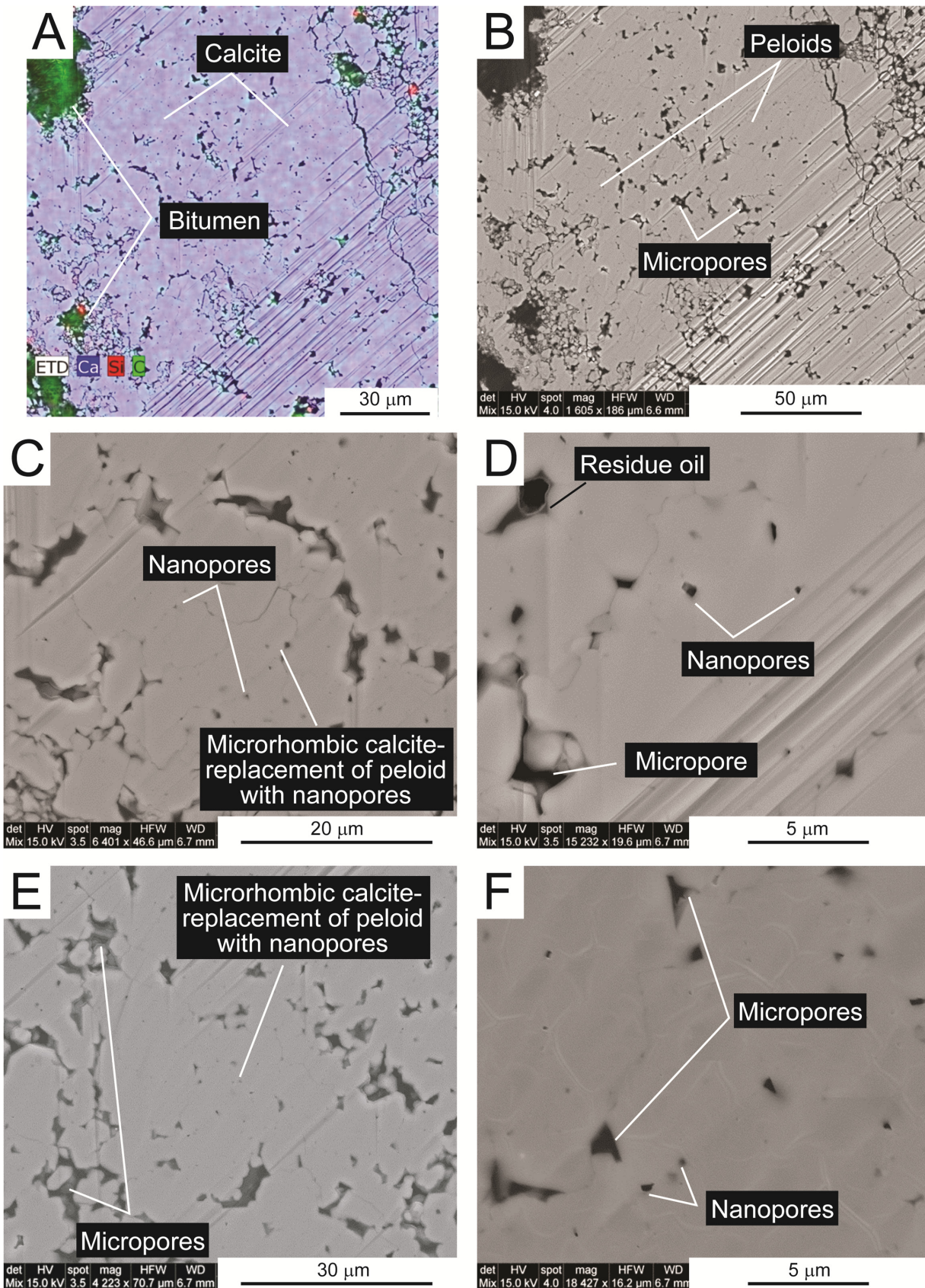
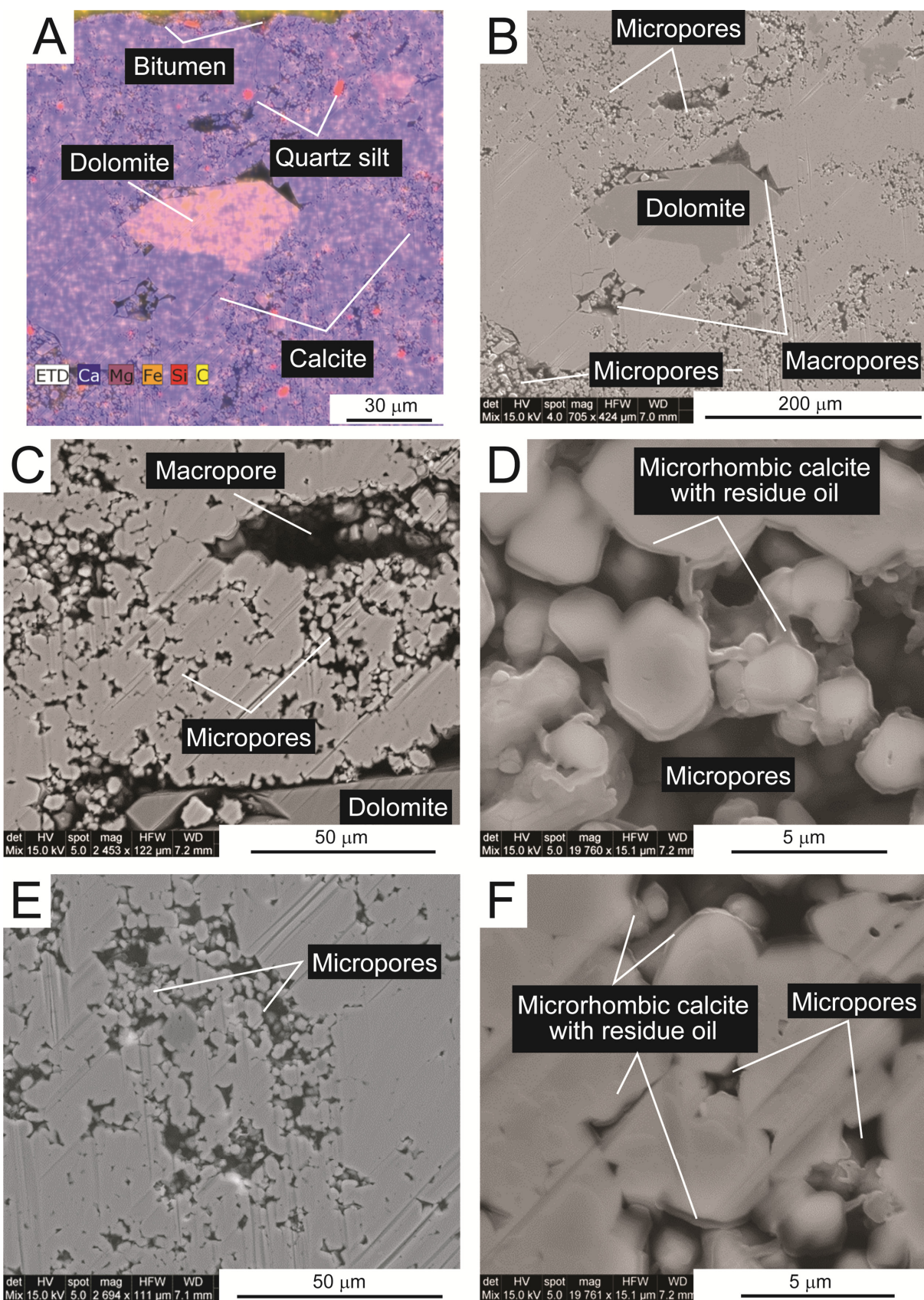
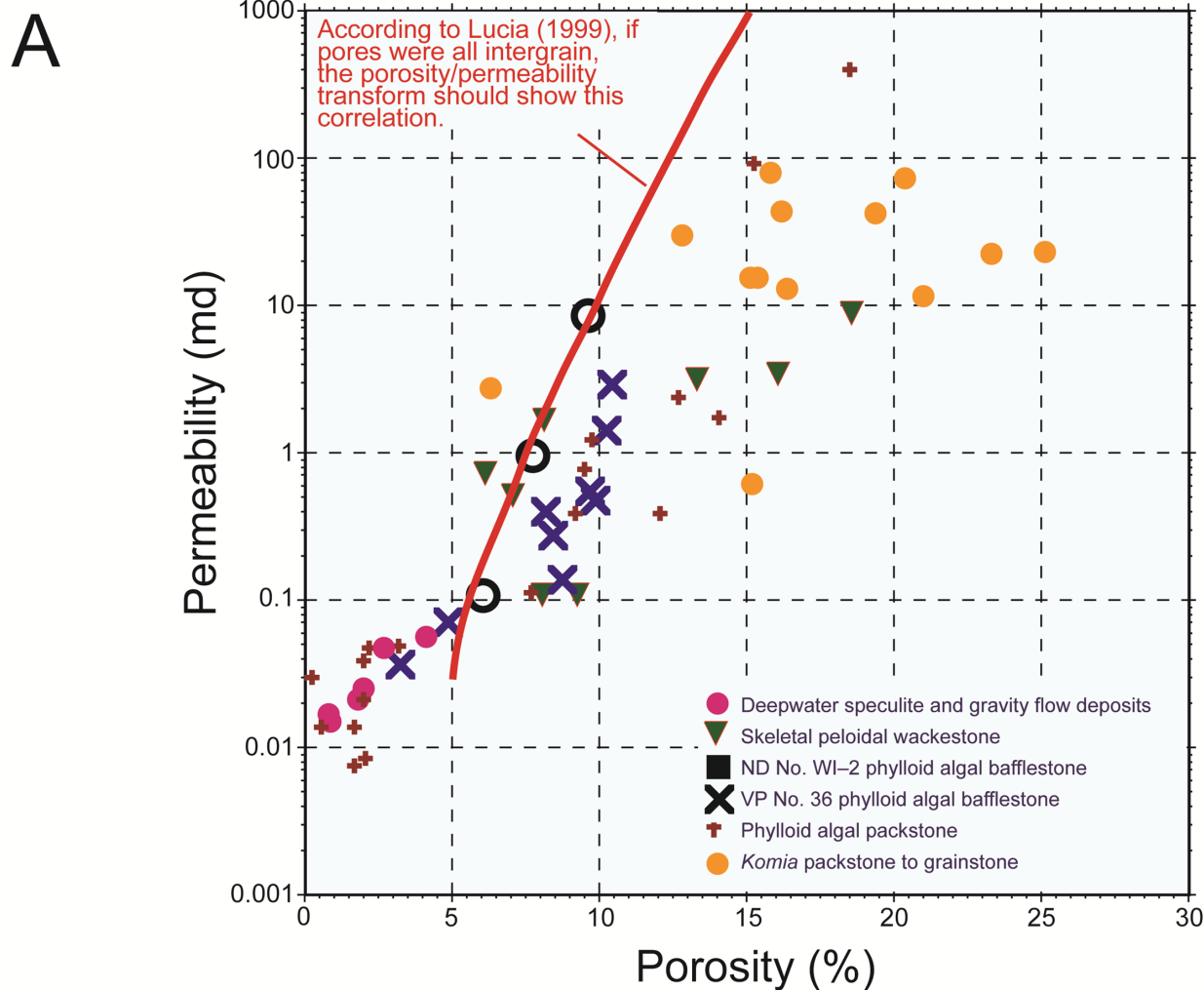


Figure 19. Examples of micropore development as shown by FESEM Ar-ion milled sample 3289 ft. (A) FESEM photograph overlain by EDAX elemental map. Sample is calcite with several pores filled with residue oil. (B) Former Mg-calcite peloids now composed of microrhomboidal calcite and associated micropores. Area between peloids contains most micropores. (C) Close-up of B showing microrhomboidal calcite replacement of peloid and associated nanopores in peloid. (D) Nanopores in peloid. (E) Former Mg-calcite peloids now composed of microrhomboidal calcite and associated micropores. Area between peloids contain most micropores. (F) Micropores filled with residue oil.



**Figure 20.** Examples of micropore development as shown by FESEM Ar-ion milled sample 3197 ft. (A) FESEM photograph overlain by EDAX elemental map. Sample is calcite with minor dolomite, quartz silt, and clay. (B) Sample showing pore network of macro- and micropores. (C) Close-up of B showing micropores. (D) Close-up of C showing microrhombic calcite with thin films of residue oil coating surfaces. (E) Former Mg-calcite grain that transformed to microrhombic calcite with associate micropores. (F) Close-up of E showing microrhombic calcite and associate micropores. Crystals coated with thin film of residue oil.



**B**

	Mean	Geom. Mean	Count	Minimum	Maximum
All porosity values	9.04		69	0.40	25.10
Deepwater speculite and gravity flow deposits	1.92		5	0.80	4.10
Skeletal peloidal wackestone	10.88		8	6.20	18.60
ND No. WI-2 phylloid algal bafflestone	8.12		12	1.60	15.00
VP No. 36 phylloid algal bafflestone	8.13		9	3.20	10.40
Phylloid algal packstone	7.03		18	0.40	18.60
<i>Komia</i> packstone to grainstone	16.08		14	2.70	25.10
All permeability values		0.74	69	0.01	370.52
Deepwater speculite and gravity flow deposits		0.02	5	0.01	0.06
Skeletal peloidal wackestone		0.93	8	0.11	8.65
ND No. WI-2 phylloid algal bafflestone		2.70	12	0.02	137.44
VP No. 36 phylloid algal bafflestone		0.34	9	0.04	3.00
Phylloid algal packstone		0.21	18	0.01	370.52
<i>Komia</i> packstone to grainstone		11.14	14	0.05	79.08

Figure 21. Reservoir-quality data. (A) Porosity versus permeability by lithofacies from core-plug analysis. (B) Descriptive statistics of porosity and permeability by lithofacies.

On Figure 21A, the porosity/permeability transform line for intergrain pore networks from Lucia (1999) is plotted. This line emphasizes that the permeabilities associated with the given porosities are generally lower than if all pores were intergrain. The lower values of permeability are interpreted to be related to the amount of moldic pores and micropores.

Figure 21B summarizes mean reservoir quality for each lithofacies. The phylloid algal facies and *Komia* facies in the Newell Dell No. WI-2 have the best reservoir quality: geometric mean permeability 2.70 and 11.14 md, respectively (Fig. 21B). The Newell Dell No. WI-2 well shows higher permeabilities because it penetrated a very porous, vuggy phylloid algal facies.

MICP is an excellent technique for characterizing pore-throat-size distribution, which provides insight into reservoir quality. As noted in Figure 22A, the three highest-porosity MICP samples have similar injection-pressure curves, with the highest-permeability sample (3267.7 ft) having the lowest injection pressure. The lowest-porosity sample (3286.4 ft) injection curve shows two populations of pore-throat sizes (Fig. 22), both in the micropore range (radii < 0.5  $\mu\text{m}$ ). Figure 22B displays the relative pore-throat-size distribution of all samples. Again, the three highest-permeability samples have similar histogram characteristics, and the lowest-permeability sample displays a two-peak population. Samples at 3267.7 ft, 3281.0 ft, and 3310.8 ft show that on average 29% (range 27% to 30%) of the pore throats are in the micropore range; sample 3286.4 ft shows that 70% of the pore throats are in the micropore range. As can be seen from the pore-throat-size histogram (Fig. 22B), nearly all the pore throats have a radius of less than 1  $\mu\text{m}$ .

Also noted from the FESEM analysis is the presence of residue oil in pore spaces (Figs. 17F, 21D, and 21F). Residue oil coats the pore walls as a film a micrometer wide or less. Some of the pores are almost completely filled with residue oil.

## CONCLUSIONS

The seven described Caddo depositional facies fit into a coherent depositional model that can be tied into higher orders of relative sea-level changes. The depositional facies varied from deeper-water spiculitic muds, to transgressive algal mounds, to shoaling conditions. Reservoir quality is strongly tied to lithofacies that were deposited in different depositional environments.

The Caddo buildup complexes are an excellent example of dual pore reservoirs comprised of macropores and micropores. The macropores are related to original interparticle and intraparticle pore space and to the dissolution of aragonite allochems such as phylloid algae. The micropores are related to the transformation of Mg-calcite to calcite. The presence of micropores must be considered when analyzing porosity/permeability transforms, hydrocarbon saturation, and reservoir reserves. Even in the macropore-rich lithofacies, micropores are common and must be taken into account when evaluating wireline logs (e.g., Pittman, 1971; Lucia, 1999).

## ACKNOWLEDGMENTS

The STARR (State of Texas Advanced Resource Recovery) program provided the major support for this investigation. We acknowledge the following members of the Bureau of Economic Geology, University of Texas at Austin, Carbonate Reservoir Characterization Research Laboratory (RCRL) for their support: Anadarko, Apache, Bahamas Petroleum, Baker Hughes, BG International Group, BHP, BP, Cenovus, Chevron, ConocoPhillips, Devon, ENXP, ExxonMobil, Husky, Ion, JAPEx, KinderMorgan, Maersk, OXY, Petrobras, PetroChina BGP, PetroChina HRIG, Pioneer, Repsol, Saudi Aramco, Shell, Statoil, Suncor, Talisman, Total, US Enercorp, Whiting, and Wintershall. Xavier Janson of the Bureau of Economic Geology reviewed the facies within the cores and offered pertinent points relative to differ-

ences in the phylloid algal mound facies. Patrick Smith of the Bureau of Economic Geology aided in the production of the FESEM photomicrographs. Greg Wahlman and Jerry Lucia edited and improved the concepts and readability of this manuscript. Publication authorized by the Director, Bureau of Economic Geology, Jackson School of Geosciences, University of Texas at Austin.

## REFERENCES CITED

- Cleaves, A. W., 2000, Sequence stratigraphy and reciprocal sedimentation in the Middle and Late Pennsylvanian carbonate-bank systems, eastern shelf of the Midland Basin, north-central Texas, in K. S. Johnson, ed., Platform carbonates in the southern Midcontinent, 1996 Symposium: Oklahoma Geological Survey, Norman, p. 227–257.
- Dunham, R. J., 1962, Classification of carbonate rocks according to depositional texture, in W. E. Ham, ed., Classification of carbonate rocks: American Association of Petroleum Geologists Memoir 1, Tulsa, Oklahoma, p. 108–121.
- Entzminger, D. J., L. Canter, M. Sonnenfeld, and S. Gardner, 2012, Waterflooding the Parks (Caddo) Field, Stephens County, Texas: American Association of Petroleum Geologists Search and Discovery Article 20127, Tulsa, Oklahoma, 29 p., <[http://www.searchanddiscovery.com/documents/2012/20127\\_entzminger/ndx\\_entzminger.pdf](http://www.searchanddiscovery.com/documents/2012/20127_entzminger/ndx_entzminger.pdf)> Last Accessed August 8, 2016.
- Forehand, M. T., 1991, Deposition and diagenesis of Caddo mud mounds, in the Breckenridge Field, Stephens County, Texas: M.S. Thesis, University of Texas at Arlington, 87 p.
- Heckel, P. H., 1986, Sea-level curve for Pennsylvanian eustatic marine transgressive-regressive depositional cycles along midcontinent outcrop belt, North America: *Geology*, v. 14, p. 330–334.
- Johnson, H. H., 1961, Limestone-building algae and algal limestones: Colorado School of Mines, Golden, 279 p.
- Kaczmarek, S. E., S. M. Fullmer, and F. J. Hasiuk, 2015, A universal classification scheme for the microcrystals that host limestone microporosity: *Journal of Sedimentary Research*, v. 85, p. 1197–1212.
- Kaldi, J. G., D. L. Boyer, and D. A. Budd, 1990, Pore-level reservoir heterogeneity in carbonates: Lisburne Reservoir, Prudhoe Bay Field, North Slope, Alaska: American Association of Petroleum Geologists Bulletin, v. 74, p. 690.
- Kopaska-Merkel, D. C., 1988, Microporosity and production potential in ooids: Mesozoic and Paleozoic of Texas: Carbonates and Evaporites, v. 2, p. 125–131.
- Lewis, E. G., 1987, A microfacies/seismic interpretation of the Caddo Lime in the Chalky Mountain Field of northwest Taylor County, Texas: Southwest Section of the American Association of Petroleum Geologists Convention Transactions with Programs, Dallas, Texas, p. 130–143.
- Loucks, R. G., R. M. Reed, S. C. Ruppel, and D. M. Jarvie, 2009, Morphology, genesis, and distribution of nanometer-scale pores in siliceous mudstones of the Mississippian Barnett Shale: *Journal of Sedimentary Research*, v. 79, p. 848–861.
- Loucks, R. G., F. J. Lucia, and L. Waite, 2013, Origin and description of the micropore network within the Lower Cretaceous Stuart City Trend tight-gas limestone reservoir in Pawnee Field in South Texas: Gulf Coast Association of Geological Societies Journal, v. 2, p. 29–41.
- Loucks, R. G., and M. Ulrich, 2015, Origin and characterization of the nanopore/micropore network in the Leonardian Clear Fork reservoirs in the Goldsmith Field in Ector Co., Texas: American Association of Petroleum Geologists Search and Discovery Article 51164, Tulsa, Oklahoma, 27 p., <[http://www.searchanddiscovery.com/documents/2015/51164loucks/ndx\\_loucks.pdf](http://www.searchanddiscovery.com/documents/2015/51164loucks/ndx_loucks.pdf)> Last Accessed August 8, 2016.
- Lucia, F. J., 1999, Carbonate reservoir characterization: Springer-Verlag, New York, New York, 226 p.
- Miller, M. C., 2001, Petrographic, petrophysical, and biostratigraphical investigation of the Caddo Limestone (Pennsylvanian),

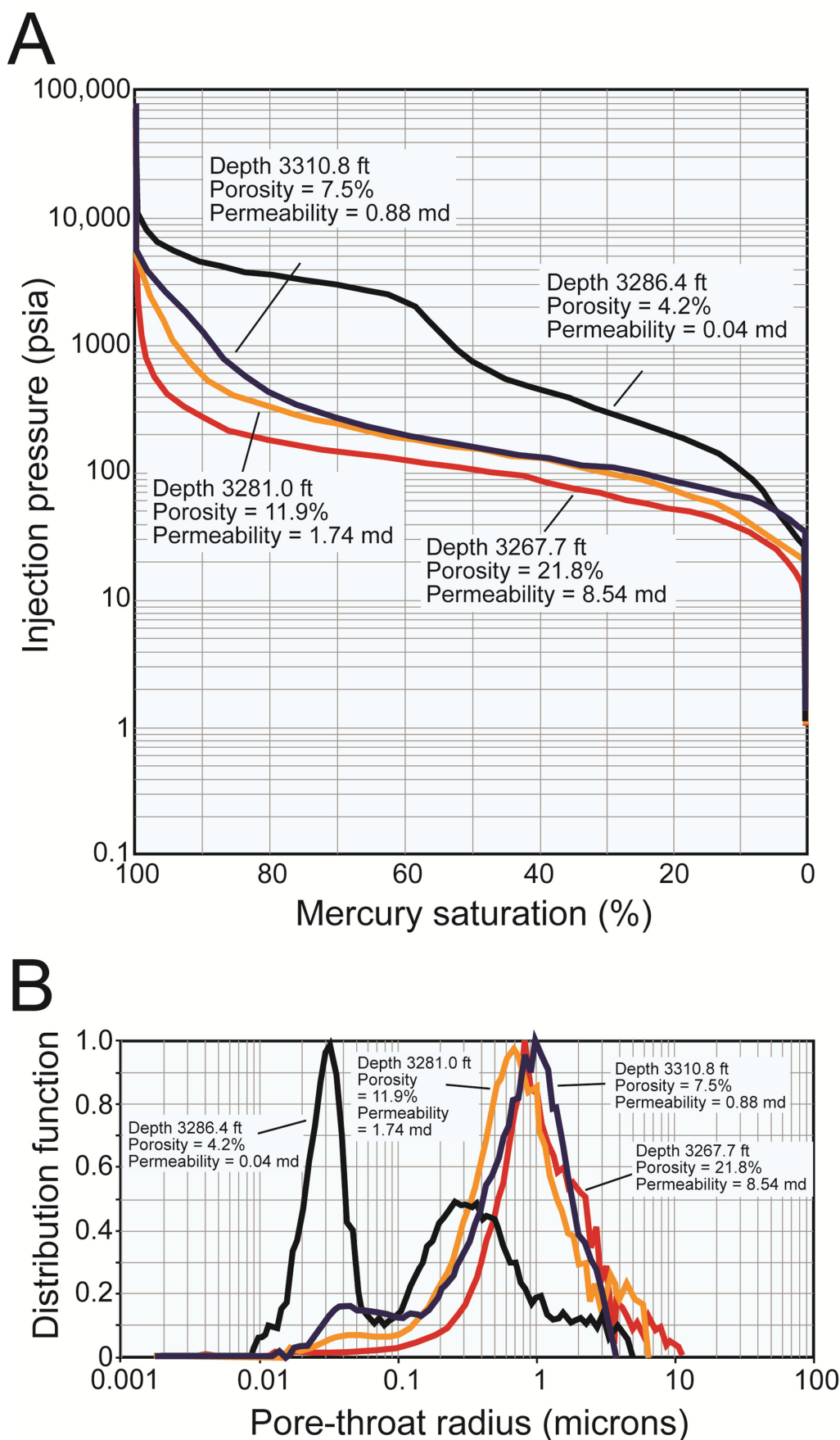


Figure 22. MICP analysis of Texas Pacific Newell-Dell No. WI-2 core. (A) Comparison of four mercury capillary injection curves with associated porosity and permeability. (B) Comparison of pore-size distribution curves as calculated by Weatherford Laboratories.

- Stephens County, Texas: M.S. Thesis, Texas Tech University, Lubbock, 129 p.
- Pittman, E. D., 1971, Microporosity in carbonate rocks: American Association of Petroleum Geologists Bulletin, v. 55, p. 1873–1881.
- Turner, G. L., 1957, Paleozoic stratigraphy of the Fort Worth Basin: Abilene and Fort Worth Geological Societies 1957 Joint Field Trip Guidebook, Texas, p. 57–77.
- Wahlman, G. P., 2001, Pennsylvanian-Lower Permian mounds and reefs in the Permian Basin (West Texas–New Mexico): Composition, evolution, distribution, and reservoir characteristics, *in* J. J. Viveiros and S. M. Ingram, eds., *The Permian Basin: Microns to satellites, looking for oil and gas at all scales*: West Texas Geological Society Publication 01–110, Midland, p. 57–64.
- Wahlman, G. P., 2002, Upper Carboniferous–Lower Permian (Bashkirian-Kungurian) mounds and reefs, *in* W. Kiessing, E. Flugel, and H. Golonka, eds., *Phanerozoic reef patterns*: Society of Economic Paleontologists and Mineralogists Special Publication 72, Tulsa, Oklahoma, p. 271–338.
- Wahlman, G. P., 2009, Diverse origins and facies of carbonate microporosity: American Association of Petroleum Geologists Search and Discovery Article 90090, Tulsa, Oklahoma, <<http://www.searchanddiscovery.com/abstracts/html/2009/annual/abstracts/wahlman.htm>> Last Accessed August 8, 2016.
- Weber, L. J., 1995, Depositional and diagenetic control of reservoir quality and continuity of the Pennsylvanian Caddo Limestone, *in* P. H. Pause and M. P., Candelaria, eds., *Carbonate facies and sequence stratigraphy: Practical applications of carbonate models*: Permian Basin Section of the Society of Economic Paleontologists and Mineralogists Publication 95–36, Midland, p. 257–286.
- Winland, A. D., 1968, The role of high Mg–calcite in the preservation of micrite envelopes and textural features of organic sediments: *Journal of Sedimentary Petrology*, v. 38, p. 1320–1325.
- Wood, S. G., 2013, Lithofacies, depositional environments, and sequence stratigraphy of the Pennsylvanian (Morrowan-Atokan) Marble Falls Formation, Central Texas: M.S. Thesis, University of Texas at Austin, 259 p.